Three Dimensional Computational Analysis of Human Burn Skin

A Dissertation submitted in fulfillment of the requirements for the Degree

of

MASTER OF ENGINEERING

in

Electronic Instrumentation & Control Engineering

Submitted by

VIVEK RASTOGI
801451029

Under the Guidance of

Dr. VISHAL SRIVASTAVA
ASSISTANT PROFESSOR, EIED

2016

Electrical and Instrumentation Engineering Department
Thapar University, Patiala
(Declared as Deemed-to-be-University u/s 3 of the UGC Act., 1956)
Post Bag No. 32, Patiala – 147004
Punjab (India)

DECLARATION

I hereby certify that the work which is presented in dissertation entitled, "**Three Dimensional Computational Analysis of Human Burn Skin**", which is being submitted by **Vivek Rastogi** in partial fulfillment of the requirements for the award of the degree of Master of Engineering in Electronic Instrumentation & Control, submitted to Electrical & Instrumentation Engineering Department of Thapar University, Patiala is as authentic record of my own work carried under the supervision of **Dr. Vishal Srivastava**. It refers others researcher's work which is duly listed in the reference section. The matter contained in this dissertation has not been submitted, neither in part nor in full to any other degree to any other university or institute except as reported in the text and references.

Place: Patiala
Date:

Vivek Rastogi
801451029

It is certified that the above statement made by the student is correct to the best of my/our knowledge and belief.

Dr. Vishal Srivastava
Assistant Professor
Electrical and Instrumentation Engineering Department
Thapar University, Patiala - 147004

Date:

Countersigned by:

Dr. Ravinder Agarwal
Professor and Head
Electrical and Instrumentation Engineering Department
Thapar University
Patiala – 147004

Dr. S.S. Bhatia
Dean of Academic Affairs
Thapar University
Patiala –147004

ABSTRACT

More than 50% of skin patients are gone through biopsies for the detection of the disease, however, with current treatment feedback, the effects and the efficacy of the treatment are generally detected several weeks/months after treatment completion. This makes the adjustment of the treatment based on early response, and identification of non-responding patients, nearly impossible. In this thesis a novel method combining optical coherence tomography with a new image processing algorithm is explored as a potential approach to detecting tissue variability.

This study involving *in-vivo* assessment of the near infra-red field attenuation coefficient of normal and burn sub cutaneous skin using swept source optical coherence tomography may indicate that burn skin are more organized by normal one. Here we represents a computational method to detect burn tissues with the goal of automatic surgical margin assessment based on OCT images. Other result demonstrates the feasibility of this computational method in the differential of burn and normal tissues.

ACKNOWLEDGEMENT

Firstly, I want to acknowledge my parents, who give me continuous love and encouragement.

I want to express my truly thanks to my advisor **Dr. Vishal Srivastava**, Assistant Professor of Electrical and Instrumentation Engineering Department, Thapar University, Patiala, who gives me invaluable guidance, support, and encouragement to conduct this project. I am honored to be mentored by him.

I express my deep sense of gratitude towards **Dr. Prakash Gopalan**, Director of Thapar Univeristy, Patiala for providing the facilities for the completion of M.E. I am also thankful to our Head of Department, **Dr. Ravinder Agarwal** as well as PG coordinator, **Mr. Nirbhowjap Singh**, Assistant professor, Electrical and Instrumentation Engineering Department.

I would like to thank the entire faculty and staff of Electrical and Instrumentation Engineering Department and my friends who devoted their valuable time and help me in all possible ways towards successful completion of this work. I thank all those who have contributed directly or indirectly to this work.

I would also like to thank **Dr. Krishna Dalal**, department of bio-physics in All India Institute of Medical Science, New Delhi, whose advice and insight have helped propel this work forward.

I would like to express my sincere gratitude to all!

VIVEK RASTOGI

TABLE OF CONTENTS

LIST OF TABLES

LIST OF FIGURES

LIST OF ABBREVIATIONS

Main symbols and notations used in this study are listed below. Sometimes a symbol may have alternate meaning, but in such a case; the context is sufficient to avoid confusion.

CCD	Charge Coupled Device
CT	Computed Tomography
FD-OCT	Fourier Domain Optical Coherence Tomography
FDML	Fourier Domain Mode-Locked
GLCM	Gray Level Co-Occurrence Matrix
MRI	Magnetic Resonance Imaging
MZI	Mach-Zehnder Interferometer
OCT	Optical Coherence Tomography
PET	Positron Emission Tomography
SLD	Superluminescent Diode
SPECT	Single Photon Emission Computed Tomography
SS-OCT	Swept source Optical Coherence Tomography
SVM	Support Vector Machine
TD-OCT	Time Domain Optical Coherence Tomography

CHAPTER 1

INTRODUCTION

1.1 Literature Review and Motivation

Now a days, most of the people in the world are suffering from cancer and skin related problems and these patients are treated with X-ray radiation therapy; however, with current treatment feedback, detection at early stages is difficult and also radiation therapy also effect other organs such as the stomach, bowel, liver and kidneys, which are very close to the area being treated. That is why we need to adjust the treatment, based on early response, identification & detection of non-responding patients, nearly impossible. In this thesis a novel method optical coherence tomography may allow the tracking of microstructural changes in cancer patients and this help in the treatment based on early response.

Optical coherence tomography, which is commonly known as OCT, is a modern non-invasive, non-contact, non-destructive optical imaging technique. It acquires cross-sectional images with high resolution in scattering media. To provide a depth profile of discontinuities it utilises the broadband light sources and interference properties of low coherence within a sample. OCT is an extension in the field of low-coherence reflectometry. It uses the broadband light source to produce interference fringes which is coupled into an interferometer. An interference pattern is obtained when the optical path difference between two arms, i.e. reference arm and sample arm, are equal to within the coherence length of the light source. Low-coherence reflectometry or optical coherence domain reflectometry make use of this fact by placing a sample in one arm, i.e. sample arm of the interferometer and a movable mirror in the other which act as a reference arm [1 – 2]. In order to observe interference mirror is scanned along reflection axis and an interference pattern is generated as mentioned above. Thus by recording various longitudinal scans at nearest lateral sites OCT creates a tomographic image.

Since the development of biomedical imaging techniques, body structure images of a patient can be produced non-invasively. Most of the imaging techniques are based on the principle of interaction of different kinds of energy with the sample tissues [3], for e.g.

ultrasonography, light microscopy, X-ray based computed tomography (CT), magnetic resonance imaging (MRI) [4 – 5], positron emission tomography (PET) and single photon emission CT (SPECT) [6].

Broadly, imaging modes can be classified as: *ex vivo* and *in vivo* imaging. In *ex vivo* imaging mode, the sample is cut out, prepared and then imaged under a microscope whereas in the case of *in vivo* imaging the tissue sample is imaged within the animal or patient body. The major difference between *ex vivo* and *in vivo* imaging schemes is that, *ex vivo* imaging schemes are mostly optical in nature and contain optical coherence microscopy, multi-photon microscopy, confocal microscopy, bright-field microscopy, second harmonic generation microscopy and fluorescence microscopy [4], whereas *in vivo* imaging schemes include ultrasound, CT, X-Ray imaging, MRI, PET and SPECT. Although, resolution offered by *in vivo* imaging systems are lesser than to *ex vivo* systems, however, real time imaging can be done easily of the patient body with less distress and quicker recovery for the long-suffering. Endoscopic instruments which are based on probe-based structures, can image *in vivo* too and by doing proper designing of a probe, optical techniques can be improved for *in vivo* imaging [7].

A comparison of capabilities among various imaging techniques is shown in table 1.1. Most of the techniques are used for detection of infection, disease management and more often biological process monitoring.

Table 1.1: A comparison of different biomedical imaging capabilities [5, 6, 8 – 11].

Imaging Techniques	***Ex vivo* Imaging Capability**	***In vivo* Imaging Capability**	**Used for Disease Management**	**Used for Biological Process Monitoring**
Optical Imaging	✓	✓	✓	✓
Ultrasound Imaging	-	✓	✓	✓
X-ray Imaging	-	✓	✓	✓
Magnetic Resonance Imaging	-	✓	✓	✓
Nuclear Imaging (e.g. SPECT and PET)	-	✓	✓	✓

Optical imaging techniques, in comparison to others, are the most adaptable techniques and capable of *in vivo* as well as *ex vivo* imaging with a high resolution. Today, these innovative

biomedical imaging techniques such as PET and SPECT are developing new paths in the improvement of sophisticated imaging technologies [3].

In disease management, wall motion abnormalities of the heart for the duration of stress can be evaluate by faster MRI sequences [6] and can also image carcinoma [12]. PET is used for the imaging of tumors non-invasively, not even primary tumors as well as distant metastases [6, 13] can be identified. At the present period of time 4-dimensional (i.e. 3D and dynamic) re-construction of tissue structure can be done anywhere in the body by multi-detector CT [14]. Whole body imaging systems are very sensitive and powerful; however they are usually employed, when tumors have achieved a certain size and cancer has already happened. Due to limited resolution it is not used for early cancer detection for e.g. the resolution of Positron Emission Tomography is 3 mm [5].There is much area for the improvement of non-invasive optical technologies with depth-resolved and high resolution and the capability to differentiate early dysplastic variations in epithelial cells for e.g. cell nuclei enlargement.

A brief comparison of the various medical imaging techniques based on the operational requirements, technical specifications, advantages and disadvantages are shown in Table 1.2.

Table 1.2: Comparison of various biomedical imaging techniques [4 – 6, 8 – 11, 14].

Biomedical Imaging Techniques	Imaging Depth	Imaging Resolution	Radioisotope/ Fluorescence Marker	Advantages	Disadvantages
Confocal Microscopy	<250 µm	1µm	Fluorescence Marker	i. Highest imaging resolution, suitable for cellular and molecular imaging. ii. Can perform real time imaging. iii. *In vivo* (probe based) and ex *vivo* imaging capability.	i. For *ex vivo* imaging, sample biopsy and Preparation needed. ii. Limited imaging depth.
Optical Coherence Tomography	2-3mm	2-15 µm	None	i. Ability to perform structural and functional imaging. ii. Imaging resolution is close to confocal, sufficient for cellular imaging. iii. Can perform real - time imaging. iv. Able to perform *in vivo* imaging.	Imaging depth is limited.

Ultrasound Imaging	>10cm	150 µm(10 - 150 µm High freq. Ultrasound)	None	i. Reasonable depth and good resolution for tissue level imaging. ii. Can perform real time imaging. iii. Contrast agents optional. (E.g. Micro bubbles)	i. Imaging depth dependent on frequency used. ii. Contact with conducting medium is needed. iii. Cannot image through air. iv. Inability to distinguish between benign and malignant tumors.
Computed Tomography (X-Ray)	Whole Body	300 µm	Contrast Dye	i. Can perform whole body and near real time imaging	i. High dosage of ionizing radiation. Not suitable for young patients. ii. Inadequate contrast of x-ray imaging for dense breasts, to distinguish between benign and malignant tumors.
SPECT Imaging	Whole Body	3mm	Radioisotope	Ability to image physiology and function.	Harmful radioactivity of radioisotopes
PET Imaging	Whole Body	3mm	Radioisotope	Ability to image physiology and function.	Harmful radioactivity of radioisotopes
MRI	Whole Body	1mm	None	i. Can perform whole body imaging. ii. Excellent soft tissue contrast.	Inability to provide specific chemical information and any dynamic information like real-time tissue response to treatment.

Ultrasound [15 – 17] and Magnetic resonance imaging [18 – 19] are very useful in the diagnosis and monitoring of the tendon injury. Also ultrasound resolution is much better than MRI; it's usual imaging resolution of around ~150 µm [5] which is far good enough compared to the 1 mm resolution of MRI for monitoring tendon injuries [10]. Moreover ultrasound monitoring of tendons can be accomplished in real-time via a low-cost system than that of MRI. Besides this, for ultrasound imaging, small high- frequency probes are required whose operating range varies from 7.5 to 15 MHz which are not widely accessible. Hence the image quality and steadiness is also dependent upon operator. Advanced techniques for tendon healing process like bright-field microscopy, stem cell therapy [20] and other optical techniques usually used for monitoring of stained tissue segments which having a considerably good resolution as compared to ultrasound imaging. With optical techniques tissue structures and cellular morphology can be noticeably observed. Hence, a depth-resolved, high resolution, non-invasive imaging technology is required for better examine of healing process by the monitoring the effect of stem cells and also to recognise injured tendon because histological assessment process, i.e. the study of the microscopic anatomy of cells and tissues is time consuming and subsequently intensive care is not possible of the healing progression in the same tendon over an extended period of time.

The field of OCT has been developed at a fast rate since its beginning due to parallel improvements in many areas of technology. Developments in optical techniques, light sources, data acquisition and computing techniques have all permits OCT to developed rapidly and discover wide functional areas, specifically in biological and medical uses. Now, video-rate monitoring is done at close to micron axial resolution [21] with rapid 4-dimensional scanning. This becoming a new possibility for OCT. OCT found new applications in the medical field, not even in ophthalmology but as well as in the field of cardio-vascular surgery.

1.2 An Overview of Tissue Analysis

Tissue analysis offers an understanding of the functional and structural connections of tissues. Analysis of tissues consists of the imaging and also provides information, facts and necessary data on tissue state which is precarious to the development of biomedical applications. Various applications related with tissue analysis are shown in figure 1.1. Primarily, disease management mainly emphasis on disease diagnosis and detection, which is a key factor of tissue analysis [6].

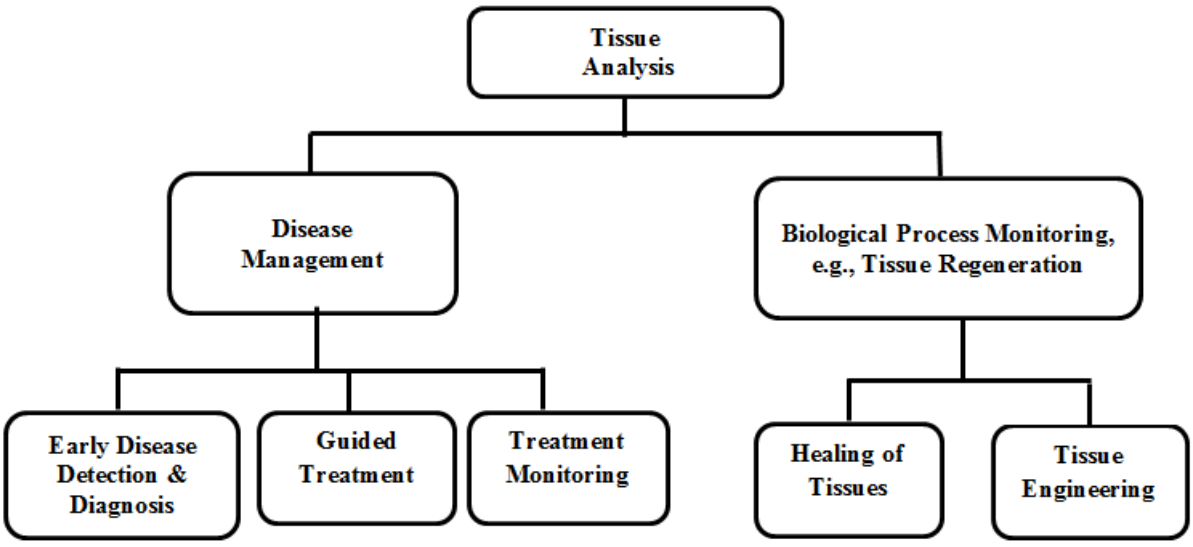

Figure 1.1: Tissue analysis applications [6, 20, 22 – 25]

Biological process monitoring is one more important application for analysis of tissue which includes the imaging of tissue regeneration in the process of tissue healing. Essentially, tissue healing consists of muscle injury due to loading stress, wound healing due to burns [24], sharp force trauma and blunt force trauma [25]. Latest advancements in the tissue healing methods, for accelerated healing, include the usage of stem cells [20]. Tissue engineering focuses on regenerative medicine in which biological alternatives are produced to restore, regenerate or replace defective tissues. Tissue engineering is a worthwhile alternative choice for organ or tissue replacement therapy [22 – 23].

In the study of relationship between anatomic arrangements of structure to biologic function and to identify and to offer necessary treatment for disease, visualization plays very important role. Conventionally, these visualizations can either invasive, for e.g. biopsy or surgery, or non-invasive which require widespread mental reconstruction. However, these histological three-dimensional (3D) and four-dimensional (4D) computational medical-imaging techniques reduce the need for physical surgery, dissection and biopsies which provides new alternatives for biological investigations, medical diagnosis and treatment [14].
Accuracy and response time are two major advantages of these non-invasive refined medical imaging techniques, through which identification of disease and trauma has transformed into better patient care timely [6]. However, further developments in biomedical imaging techniques can develop the understanding between the functional and structural relationships of tissues and cells, thus enabling the diagnosis of disease and clinical management and their corresponding reflections to therapy.

1.3 Optical Imaging Modalities

Figure 1.2 shows the various optical imaging techniques. Reflection methods are the most appropriate techniques for thick tissue or *in vivo* optical monitoring, as the tissue models are normally too dense for transmission-based monitoring. The reasons for the extensive usage of optical imaging for biological tissue include [8, 26 – 27]:

(i) For biomedical applications, photons deliver non-ionizing and safe radiation.

(ii) Real – time monitoring.

(iii) For *in vivo* imaging, optical systems can be combined into endoscopes by the use of fiber-based systems.

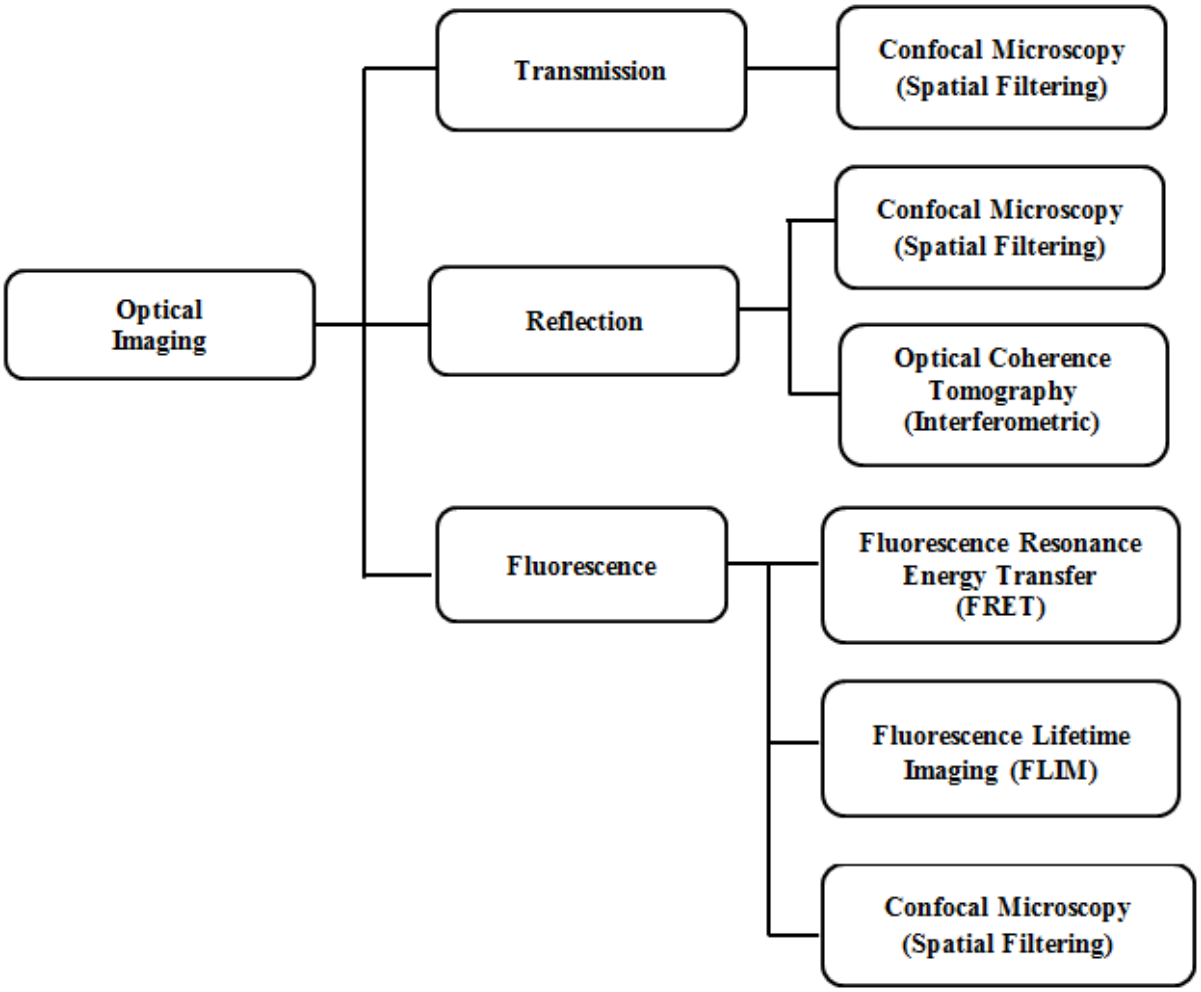

Figure 1.2: Different optical imaging methods [4].

With the following mechanisms, optical imaging delivers structural as well as functional information with high resolution [8, 26 – 27]:

(a) The size distribution information of optical scatterers is provided by optical scattering spectra, for e.g. cell nuclei.

(b) Structurally anisotropic tissue components information is provided by optical polarization, for e.g. collagen, muscle fiber.

(c) Because of Optical Doppler Effect, blood flow information is provided by optical frequency shifts.

(d) Biochemical information is provided by optical spectra which are based on Raman scattering, absorption or fluorescence.

(e) Biomarkers contrast for the molecular based imaging is provided by targeted contrast agents' optical properties.

(f) Optical spectroscopy allows simultaneous detection of several contrast agents.
(g) Eye's optical transparency offers a distinctive opportunity for high resolution monitoring of the retina.

As, most of the optical imaging methods uses a microscope, hence the objective lens used to provide the possible spatial resolution. As biological tissues have strong scattering in optical radiation, hence the depth of penetration provided by light in the tissue sample is limited. Besides this, skin or tissue sample have lower absorption, fluorescence and scattering properties in the visible region as compared in near-infrared region, hence soft tissues shows an optical window in the near-infrared band [8].

CHAPTER 2

OPTICAL COHERENCE TOMOGRAPHY

OCT measures optical reflections and acquires sub-surface images, from within the skin/tissue sample by interferometrically. Since the speed of light of propagation is very much high as compared to speed of sound waves, hence light packets backscattered from skin/tissue sample's scatterers cannot be recorded electronically as in ultrasound. Therefore, the reconstruction of depth resolved cross-sectional OCT image depend upon the propagated back – scattered energy photon's optical path length whose direction of propagation is in the z- direction, i.e. axial-direction (figure 2.1) with respect to x-direction (i.e. transverse scanning)[28]. Low-coherence interferometry is employed in order to demodulate light's optical delay after propagation with in the tissue as well as back scattering from skin/tissue sample's scatterers.

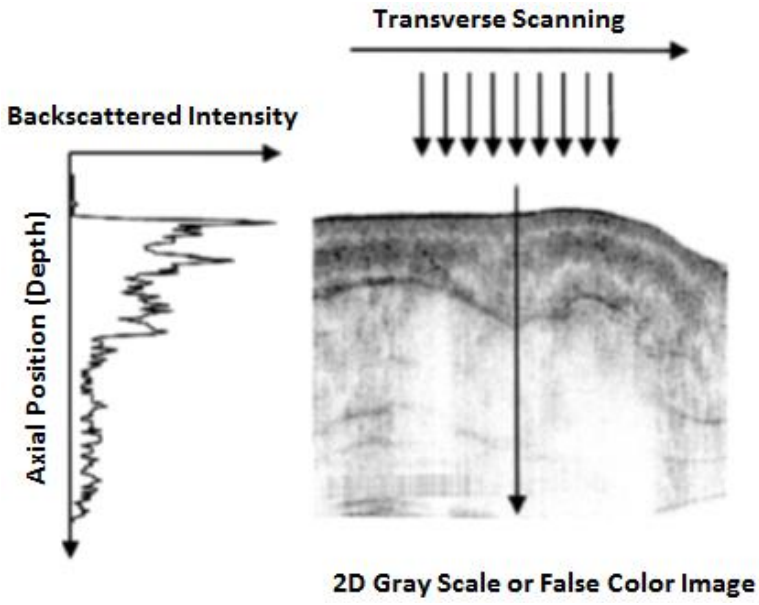

Figure 2.1: Image reconstruction in OCT [29].

Essentially, there are two major techniques for obtaining OCT images: time-domain (TD-OCT) and Fourier-domain (FD-OCT). As both techniques are follow the principle of low-coherence interferometry but still both are fluctuating from each other in terms of detection and demodulation of interference fringes to provide depth-resolved spatial information. Spectroscopic OCT, Doppler OCT and Polarization-Sensitive OCT are the major functional

extensions of OCT which can be associated with either Time Domain OCT or with Fourier Domain OCT as shown in Figure 2.2.

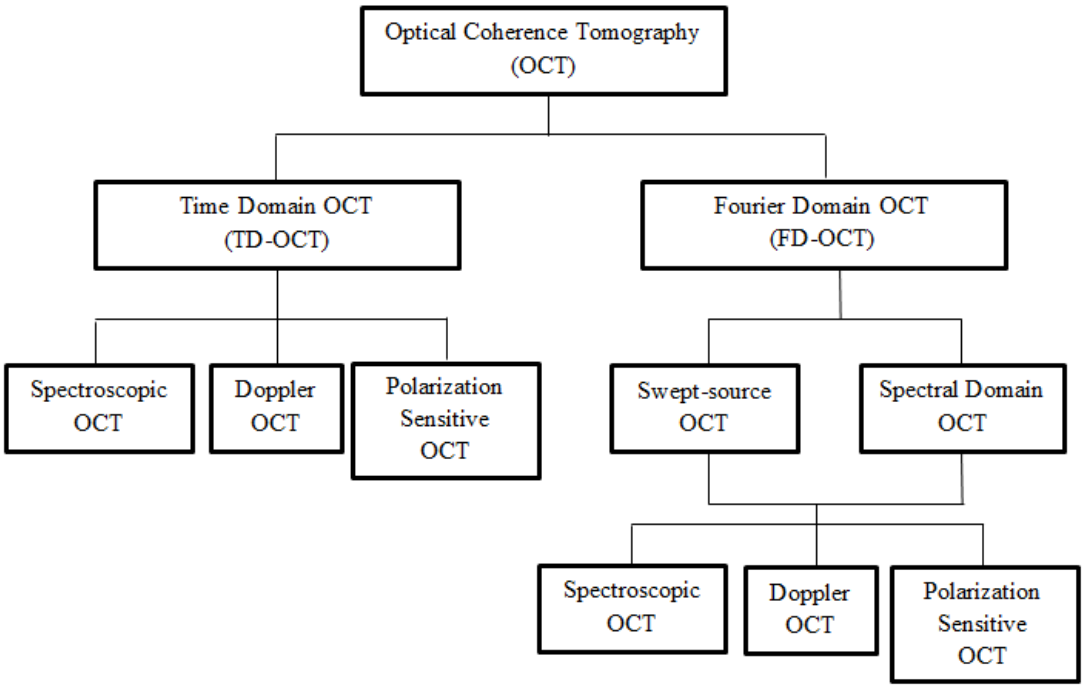

Figure 2.2: Extensions of OCT modalities [4].

TD-OCT systems is based on the basic configuration of Michelson interferometer in which a reference mirror in one arm and sample is in other arm is used. From the light source (SLD) light is divided by a coupler in such a way that the most of the light travel through the sample mirror and rest going to the reference mirror. The reference mirror moves continuously in order to scan various depth profiles within the tissue. Thus, the TD-OCT system provides an optical pathlength difference between backscattered light and reference beam from the sample [4]. At a given location, an interference pattern is generated when the difference of optical path length between two arms is within the range of coherence length of the low-coherence light source light source, the light which is backscattered from the sample as well as the light which is reflected from the reference mirror coupled together. This interference pattern contains necessary information regarding various depths profile at the tissue, which is known as A-scan and a group of A-scans is further known as B scan, which helps in reconstruction of a depth resolved cross-sectional image of skin/tissue sample. Thus, by scanning B scans and C scans in transverse direction a 3D OCT image can be obtained [30].

Fourier-domain OCT (FD-OCT) is another technique of determining the backscatter signal from a tissue sample. The basic principle of FD-OCT is based on the Wiener-Khinchin theorem. According to this theorem Fourier relationship occurs between the autocorrelation function and the power spectral density of a process [31]. In other words Fourier domain OCT (FD-OCT) examines the interference signal spectrum which gives depth information which is the autocorrelation of sample and reference arm light fields. The amplitude is representative of the reflectivity of that layer and the frequency is representative of the depth of the layer. The complete A-scan (depth structure) is acquired synchronously with the spectral information and no further depth scanning of reference arm is required. FD-OCT systems achieve necessary information of depth profile by examining the interferogram spectrum. Then Fourier transformation of the interferogram spectrum provides the depth resolved information [32]. Since in FD-OCT there is no need of coupling of electronic detection bandwidth and reference mirror scanning, hence the sensitivity increases in comparison to TD-OCT which facilitates a fast A-scan rate with high image performance [33 – 37]. This high speed imaging advantage of FD-OCT permits 3D tissue visualization as well as *in vivo* study of functional tissue characteristics [38].

In contrast with other clinical imaging techniques like CT, MRI, confocal microscopy and ultrasound imaging the gap of resolution and imaging depth between confocal microscopy and ultrasound imaging is filled by optical coherence tomography, as shown in figure 2.3.

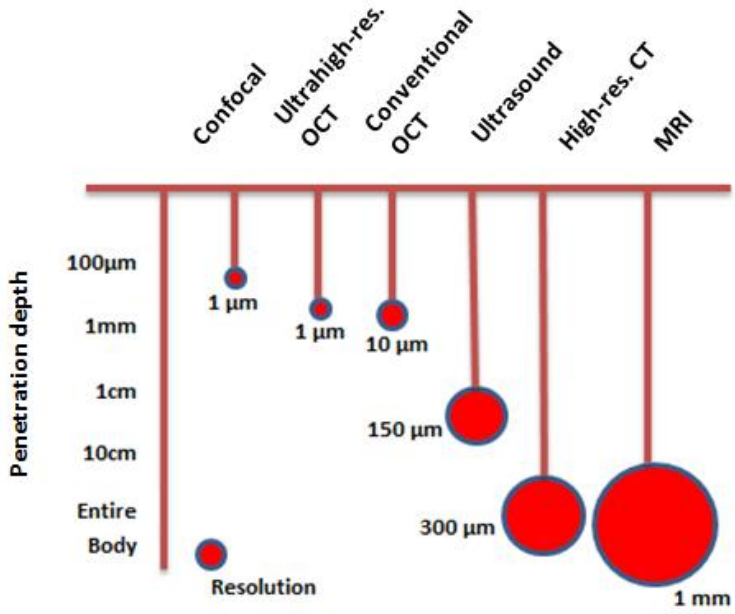

Figure 2.3: Comparison of imaging capability of OCT with other imaging modalities. The pendulums' lengths depict the depth of penetration while the disks' sizes depict the resolution of each modality [39].

Although, CT and MRI both are non-invasive and non-destructive modalities in their working operation, but they do not provide the resolution as high as offered by OCT [40]. In addition, MRI and CT systems are also more expensive and both are require highly trained professionals for day-to-day routine operation. In CT method highly ionizing radiation is used for imaging purpose which is also a health concern. A fluorescent marker is used in confocal fluorescence imaging as contrast agent into a sample whereas there is no need for sample preparation in OCT. Even though similar to confocal microscopy, OCT also uses backscattered photons detection method, through heterodyne gain detection method the overall sensitivity can be increased also signal-to-noise ratio (SNR) can be achieved up to 105 dB [37] as compared to conventional confocal microscopes. As OCT is an optical imaging technique, hence it can also be used with endoscopic probes which permit imaging of biological structure throughout the surgical procedures [7].

Since the imaging of tissue structural information is highly dependent upon the amount of backscattered light, which is also affected by various factors such as refractive index and cellular density, hence the contrast of OCT images is also effected that makes the differentiation of various tissue sample microstructures to challenging [31, 41]. It is very difficult to quantify the small variation in tissue scattering properties between normal and pathological condition at very early stage of a disease. OCT has been usually employed where the application of OCT is used for the detection of early cancer condition in epithelial tissue is shown [28, 42]. Identification of more contrast method is one of the most challenging job in order to extend the clinical usage of OCT which can facilitate physiological information as well as morphological structure too[41]. Although, different kind of OCT imaging modalities of tissue physiology, such as Doppler OCT (DOCT), Spectroscopic OCT and Polarization sensitive OCT (PS-OCT) have been developed. Doppler OCT combines the Doppler principle of operation with OCT in order to acquire high-resolution images of tissue sample and blood flow all together [43 – 46]. Polarization sensitive OCT integrates polarization sensitive detection mechanism with OCT to obtain tissue birefringence [44]. Spectroscopic OCT uses broadband light source in order to obtain backscattered light spectrum by depth dependent analysis [45]. Spectroscopic differentiation is only possible when either two or more than two scatterer in a sample backscatter differently in the range of OCT light source wavelength. Small scatterers provide rise at small frequency spectral modulations whereas larger scatterers provide large frequency spectral modulations, as shown in Figure 2.4.

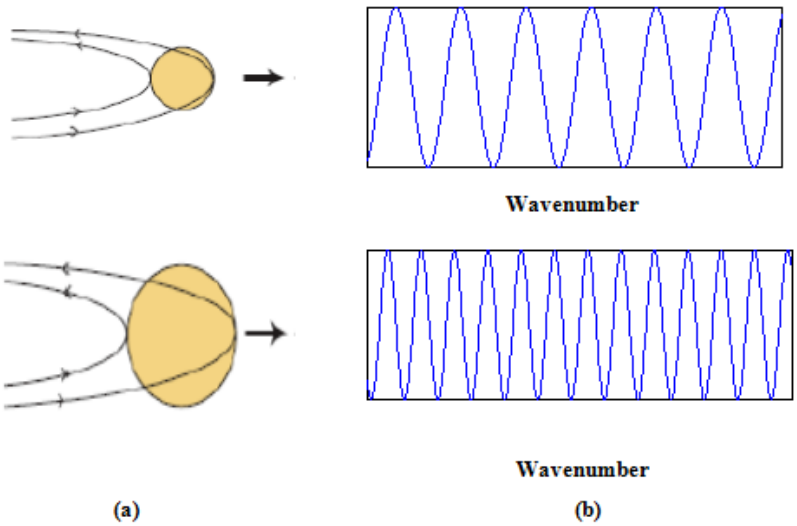

Figure 2.4: (a) Cell nuclei indicate incident and scattered fields. (b) Interference spectrum and wave number which depends upon the oscillations due to interference [43].

At early stages detection of cancerous cells is dependent on the position and difference between neoplastic and dysplastic cells by identifying and recognizing cell nuclear morphology [45]. As mucosal and skin tissues epithelial layers seems to be well within the measurable range of OCT, therefore a mechanism like Spectroscopic OCT plays a significant role in the early detection of variation of infected cellular structure by means of the differentiation and identification of tissue scatterer structure.

Moreover, healing of skin tissues and tissue growth like biological process monitoring can be done by using Spectroscopic OCT which provides the information of cell proliferation in an injury or burn site. In addition, Polarization sensitive OCT and Doppler OCT has another capabilities like tomographic imaging of collagen and detection of blood flow direction, respectively. Table 2.1 gives a comparison of merits and demerits of FD-OCT with Spectroscopic OCT.

Table 2.1: Comparison of merits and demerits of FD-OCT and SOCT [33, 34, 37].

	Fourier-Domain OCT	Spectroscopic OCT
Advantages	i. Depth-resolved structural imaging. ii. Non-invasive (no contact with sample needed). iii. 3D volumetric imaging. iv. High axial resolution (2–15μm). v. Real time imaging. vi. Non-ionizing radiation (Near-infrared light). *vii. Ex vivo* and *in vivo* imaging modalities available.	i. Differentiation of scatterer sizes based on spectral analysis of back-scattered light. ii. Improved contrast of OCT images due to better differentiation of scatterers. iii. Qualitative and quantitative analysis of scatterers offer better understanding of biological phenomena.
Disadvantages	Limited imaging depth (<3 mm).	Extensive computational processing needed.

2.1 OCT Fundamental

Figure 2.5 shows the schematic diagram of OCT which is based on Michelson interferometer. The light beam coming from the light source is divided into reference beam $\overrightarrow{Er}$ and sample beam $\overrightarrow{Es}$. The reflected light from the reference mirror M1 at a distance Z_r and the reflected light from the sample at a distance Z_s with respect to beam splitter both are combined at the beam splitter and an interference will occur only when the path difference between reflected light from the reference mirror M1 and reflected light from the sample arm M2 are within the coherence length or $Z_r \sim Z_s \leq l_c$, where l_c represents the coherence length. The depth resolved information can be extracted from these interference fringes.

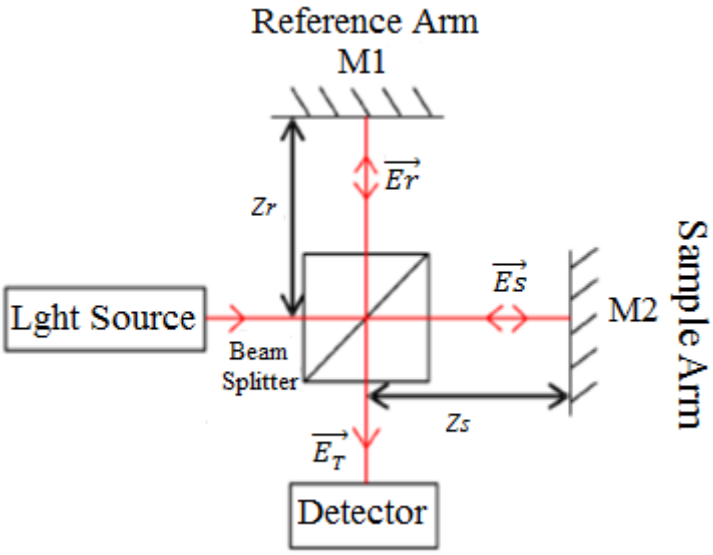

Figure 2.5: Schematic of Michelson interferometer [47].

The E - field of a light wave $\vec{E}(t)$ can be defined as [48]:

$$\vec{E}(t) = \left[E_0 e^{-j(\vec{K}.\vec{r}-\omega t)}\right].\hat{e}_r \tag{2.1}$$

where,

E_0 = wave amplitude, $\vec{K}$ = wave vector, $\vec{r}$ = position vector, ω = frequency of the wave and $\hat{e}_r$ = unit vector in the direction of wave propagation.

The reflected light wave $\overrightarrow{Er}$ from reference mirror M1 can be denoted by:

$$\overrightarrow{E_r}(t) = \left[E_r e^{-j(k.2z_r-\omega t)}\right].\hat{e}_z \tag{2.2}$$

where,

k = $\frac{2\pi}{\lambda}$ is the propagation constant, λ = wavelength of light source, $\hat{e}_z$ = unit vector in z-direction. Similarly, the reflected light wave $\overrightarrow{Es}$ from sample arm mirror M2 is given as:

$$\overrightarrow{E_s}(t) = \left[E_s e^{-j(k.2z_s-\omega t)}\right].\hat{e}_z \tag{2.3}$$

The displacement difference z' between mirror M1 and mirror M2 is given by:

$$z' = z_s - z_r \tag{2.4}$$

The total electric field $\overrightarrow{E_T}$ at the beam splitter after $\overrightarrow{E_r}$ and $\overrightarrow{E_s}$ interfere is

$$\overrightarrow{E_T}(t) = \overrightarrow{E_r}(t) + \overrightarrow{E_s}(t) = [E_r e^{-j(k.2z_r - \omega t)} + E_s e^{-j(k.2z_s - \omega t)}]. \hat{e}_z \quad (2.5)$$

The intensity detected at the detector can be shown to be [47]:

$$\begin{aligned} I &\propto Re[\overrightarrow{E_T}(t).\overrightarrow{E_T^*}(t)] \\ &= E_r^2 + E_s^2 + 2E_r E_s \cos[k \cdot 2(z_s - z_r)] \\ &= E_r^2 + E_s^2 + 2E_r E_s \cos[2kz'] \end{aligned} \quad (2.6)$$

The two self-interference terms $2E_r^2$ and $2E_s^2$ are not used in OCT, but the cross-correlation term $2E_r E_s$ cos [2kz′] defines the interference fringes that occur when z_r and z_s are within or equal to the coherence length of the light source. Signal processing is performed on the interference term to obtain the spatial location of tissue layers.

2.2 Time Domain OCT (TD – OCT)

In TD-OCT, the axial profile I(z) of a sample can be shown to be the sum of the relative amplitudes of the sample arm at various depths z'_n [41]:

$$I(z) \propto 2\sum_{n=1}^{N} E_r(z) Es_n(z) g(z) cos[2k_0(Zs_n - Z_r)] \quad (2.7)$$

where, $K_0 = \frac{2\pi}{\lambda_0}$

λ_0 = center wavelength of a broadband light source,
N = number of tissue layers,
g (z) = degree of coherence represented by the autocorrelation of the light source spectrum,
Es_n = the back-scattered E-field from interfaces.

In early stages of development, for coronary artery and retinal imaging first OCT system was developed which was nothing but a Time Domain OCT system. Imaging of retina is a clinical example of transparent tissue whereas coronary artery belongs to a turbid tissue [49]. Figure 2.6 (a) shows the execution of imaging by a fiber-optic based Michelson interferometer using a broadband or low-coherence light source. The advantage of using fiber-optic is that the

system becomes more robust and compact which further enhanced its application in various clinical and biomedical imaging methodologies. Ultrafast laser sources for example Ti:Sapphire lasers or Superluminescent diodes (SLD) used for generation of Low coherence light [41]. One interferometric arm holds a modular probe which collects the backscattered light by focusing the light on the tissue sample and hence scans the whole sample, whereas the second interferometric arm with a translating mirror is used in a reference path. Figure 2.6 (b) depicts a simulated sample interferogram through three optical interfaces. Interference occurs whenever the reference arm or mirror moves to the equal amount of the next layer of the sample. Detection and demodulation of interference fringes takes place by electronic means in order to provide a measurement of magnitude as well as measurement of echo delay time of backscattered light from tissue structures.

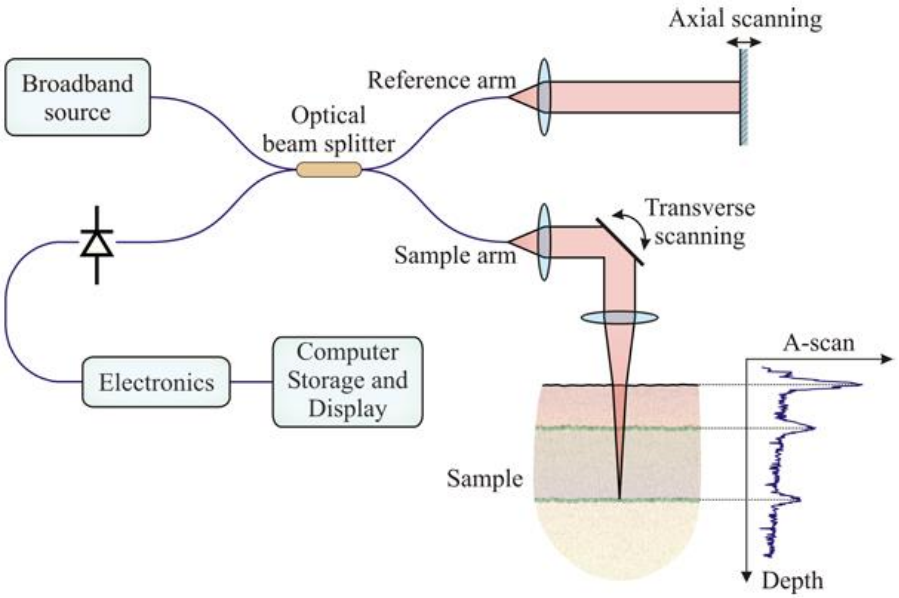

(a)

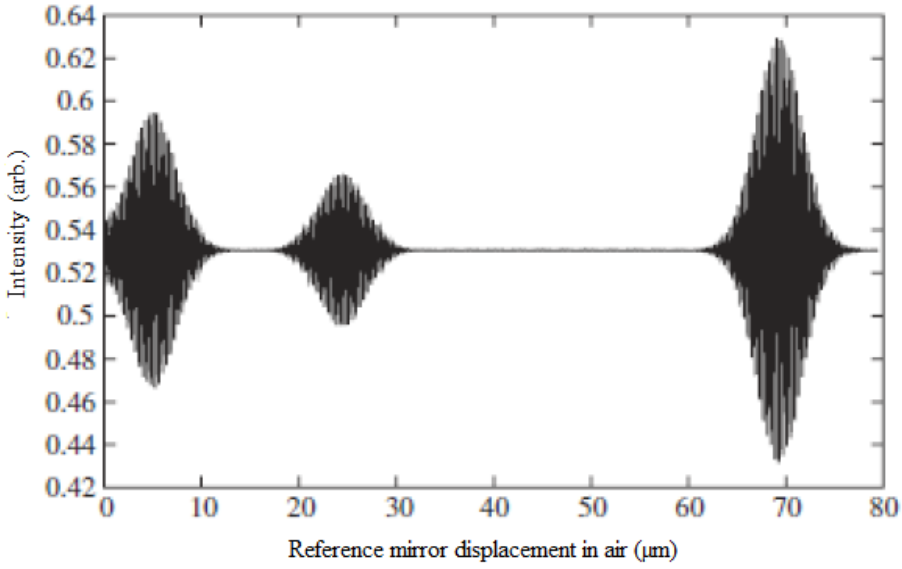

(b)

Figure 2.6: (a) Schematic of a Time Domain OCT (TD-OCT) system [50] and (b) simulated sample interferogram through three optical interfaces [47].

Low-coherence interferometry provides a high resolution of optical echoes in terms of femtosecond that resembles to measurement of distance in micron-scale which simply cannot be achieved by direct time-of-flight electronics. In TD-OCT, 2-dimensional depth resolved cross-sectional tomographic images of internal microstructure of tissue can be reconstructed by performing several axial measurements of backscattered light and by doing continuous scans of optical beam at multiple transverse positions. Hence, obtained data set represents a 2D array of optical backscattering within a tissue sample, which can be digitally processed and displayed by means of a 2-dimensional gray-scale/false-colour image.

2.3 Fourier Domain OCT (FD - OCT)

In early 1995, Fourier domain detection technique was developed [33 – 38, 51]. In this method depth information of tissue is obtained by axial scan (A-scan) without any mechanical movement of reference arm. In spectrometer, the acquisition speed of tomographic imaging is dependent upon the scan rate of arrays of CCD (charge coupled device) detectors. Even though, FD-OCT systems have a much higher scanning speed as compared to TD-OCT systems [34, 51]. An adjustable 2-dimensional or volumetric frame rate and approximately 312,500 A-scan/second can be realized with an ultra-high speed Fourier Domain OCT system [52], whereas in TD-OCT the scanning speed of a video rate is

limited to 4,000 A-scan/second at a frame rate approximately 32 frame/seconds [53]. Moreover FD-OCT system has a better sensitivity of more than 103 dB [37] as compared to TD-OCT system in which a sensitivity of 24 dB is achievable [53]. As there is no need of coupling of electronic detection bandwidth and scanning range [33, 38] therefore a better depth imaging of biological tissue is possible. Figure 2.7 shows a basic configuration of FD-OCT system. The detector array keeps a record of the intensity of backscattered light as a function of wavelength. The high speed imaging permits 3-dimensional tissue visualization along with the measurement of tissue properties such as vessel pulsatility and perfusion [38].

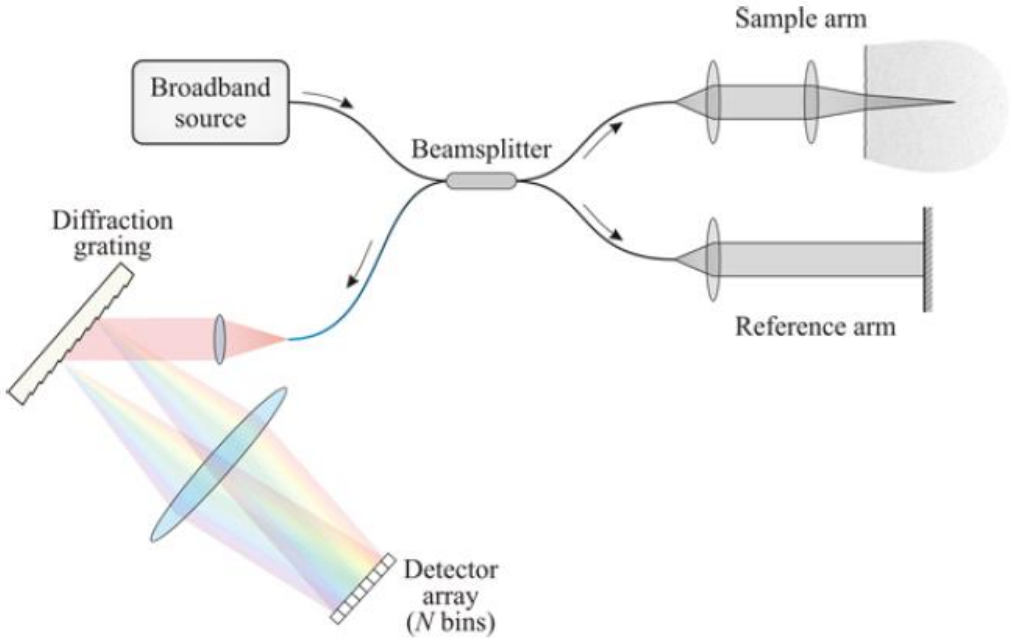

Figure 2.7: Basic configuration of a Fourier Domain OCT system [50].

The interference spectrum acquired from one axial scan of FD-OCT from a sample comprises all backscattered spectrum of different skin/tissue layers within the sample. The Fourier - Transform of obtained interference spectrum gives the knowledge of the positions and interfaces of these layers in the spatial domain. Figure 2.8 demonstrates the working operation of a Fourier Domain OCT system. The reference mirror is placed at a fixed distance of z_r and the sample tissue layers are placed at a distance of Zs_1, Zs_2 and Zs_3 from the beam splitter, respectively. At the beam splitter, the light source beam is divided into two paths and the light wave $\overrightarrow{E_r}$ reflected from reference arm interfering with the back-scattered light waves $\overrightarrow{Es_1}$, $\overrightarrow{Es_2}$, $\overrightarrow{Es_3}$ reflected from the three sample interfaces. Thus, the light waves from sample

and reference arm interfere and merged into $\overrightarrow{E_T}$ at beam splitter. The overall intensity of interference pattern is obtained by a spectrometer. Instead of using of a single photo-detector, FD-OCT system uses an array of CCD detectors as compared to TD-OCT, which records the interference spectrum that divided into its component wavelengths by a grating.

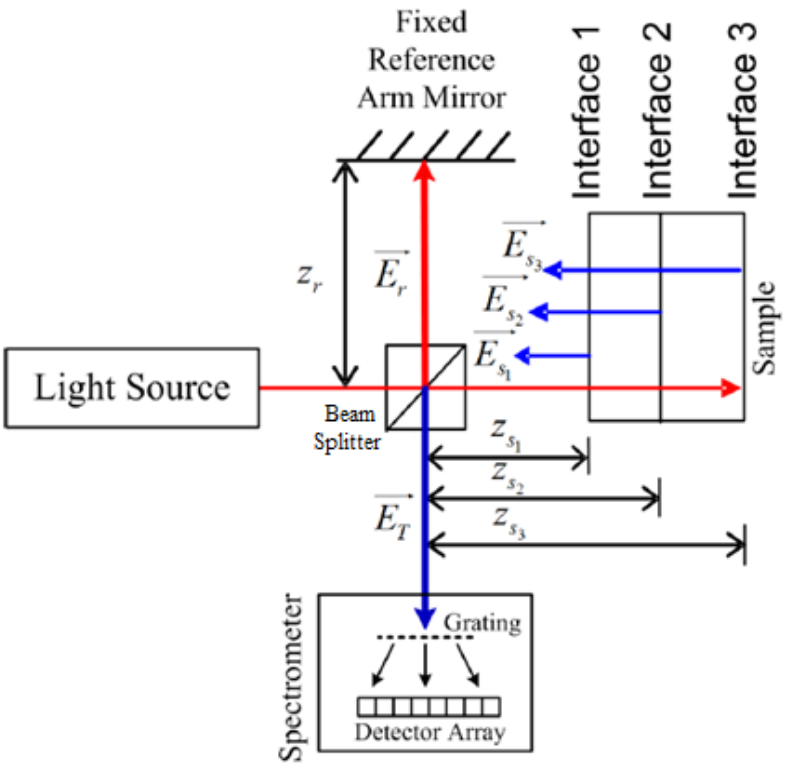

Figure 2.8: Schematic of a Fourier Domain OCT (FD-OCT) system with a sample contains three optical interfaces[41].

In FD-OCT, the interference equation remains same as equation 2.7, but here the interference profile is calculated in *k*-space i.e. in wavelength domain. At the spectrometer output, the interference intensity profile *I* (*k*) can be defined as [41]:

$$S(k)\left[E_r^2(k) + \sum_{n=1}^{N} E_{s_n}^2(k)\right] \text{ “DC Terms”}$$

$$\text{I(k)} \propto + S(k)\left[\sum_{n=1}^{N} E_r(k)E_{s_n}(k)cos\left(2K\left(z_{s_n} - z_r\right)\right)\right] \text{ “Cross – Correlation Terms”} \quad (2.8)$$

$$+ S(k)\left[\sum_{n\neq m=1}^{N} E_{s_n}(k)E_{s_m}(k)cos\left(2K\left(z_{s_n} - z_{s_m}\right)\right)\right] \text{ “Auto – Correlation Terms”}$$

where,

N = total number of interfaces in the sample,

S(k) = power spectrum of light source,

$E_r(k)$ = reflected reference arm field,

$\left.\begin{matrix} E_{s_n}(k) \\ E_{s_m}(k) \end{matrix}\right\}$ = reflected sample interface fields from different interface layers,

$\left.\begin{matrix} z_{s_n} \\ z_{s_m} \\ z_r \end{matrix}\right\}$ = spatial position of n^{th} and m^{th} sample layer and reference mirror respectively.

There are three major components arising from the analysis of spectral interferogram, that is

(i) DC terms

(ii) Cross-Correlation terms and,

(iii) Auto-Correlation terms

The "DC terms" are independent of path length. The strength of the "DC term" is depended on the reference mirror power reflectivity and the sum of reflectivity from the sample. They are filtered in OCT. In OCT imaging with the help of "cross-correlation terms" sample positions of the different interface can be identified. The "auto-correlation" terms are usually acting as an artifact in OCT which is an indication of the occurrence of interference between the various sample interfaces.

The Fourier Transform f (t) in time-domain of a frequency-domain function F(f) can be written as [54]:

$$f(t) = \int_{-\infty}^{\infty} F(f) e^{-2\pi f t}\, df \tag{2.9}$$

where $e^{-2\pi f t}$ is the FT kernel used to transform functions from one domain to another, f represents frequency and t represents time. To obtain the axial profile, *I(*z*)* , of the sample from the spectral profile, I(k) , of FD-OCT, FT is performed using a modified kernel obtained from the substitution of factors with the conventional FT kernel [41]:

$$2\pi f t \equiv 2\pi f' t' \tag{2.10}$$

where $f' = \frac{k}{\pi}$ and $t' = z$.

The axial profile I (z) can be written as:

$$I(z) = Re \int_{-\infty}^{\infty} I(k)\ e^{-2\pi\left(\frac{k}{\pi}\right)z}\, dk \qquad (2.11)$$

However, FD-OCT can be categorized into two types:-

a) Spectral OCT or Spectral Radar
b) Swept Source OCT (SS-OCT)

The common component between these two approaches is that a tissue sample is lightened with broadband light source and then the subsequent interference pattern is captured as a function of wavelength. After that, the captured signal is being processed and Fourier-transformed to provide the depth profile of the sample. The system imaging speed, resolution and sensitivity is considerably better than TD-OCT system as there is no mechanical movement of reference mirror in FD-OCT system [55 – 56].In Swept Source OCT system a specific kind of light source is used which is commonly known as swept-source laser. The output of repeatedly back and forth scans over a range of wavelengths as a function of time, which removes the essential requirement of dispersive components at the output stage and gives an input to the OCT mechanism which is spectrally varying in nature. The interference spectrum can be recorded by a single photo-detector. Then, after performing Fourier-transform, the depth profile information of sample can be obtained.

2.4 Swept Source OCT (SS - OCT)

Swept source OCT was suggested at 1997 which is also known as optical Fourier domain interferometer (OFDI) [57]. Figure 2.9 shows the basic system of SS-OCT. As comparing to previous versions of TD-OCT and FD-OCT, the major difference is that SS-OCT uses a broadband light source which provides a facility to produce an output with a time-varying wavelength instead of producing the whole spectrum at the same time. This system uses a single detector instead of using array detector, by which interference signals can be captured continuously in time. The axial resolution can be described by equation 2.15. Where, $\Delta\lambda$ represents swept source sweeping range. The ranging depth that depends upon coherence

property of light source is decided by means of immediate line-width of it. The A-scan rate of SS-OCT is highly dependent upon the swept source repetition rate not on the array detector, i.e. high the sweeping rate results faster A-scan.

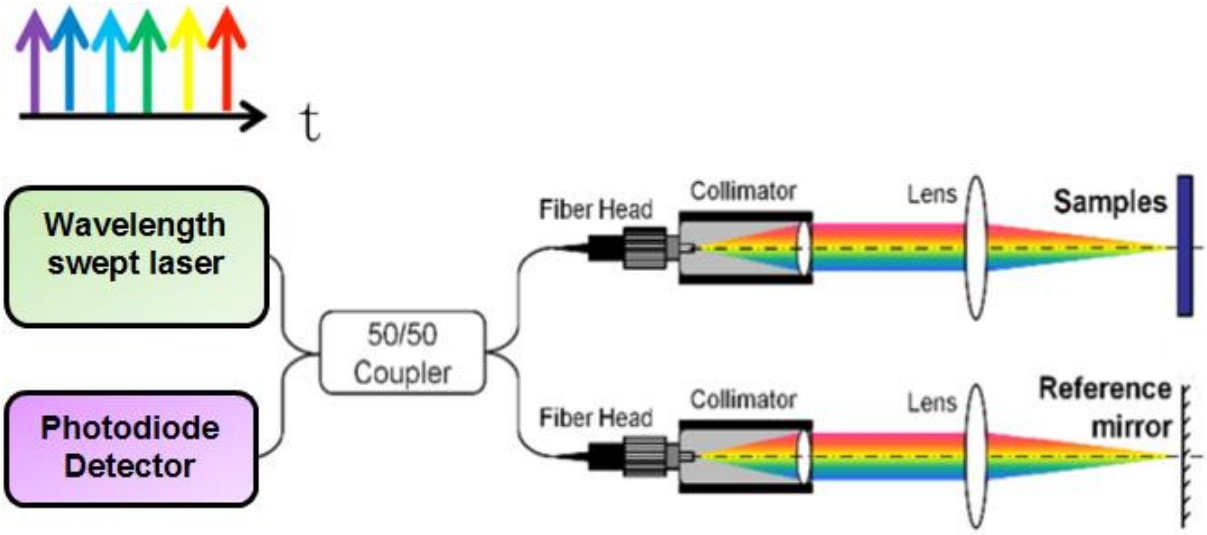

Figure 2.9: Basic block diagram of SS-OCT system [58].

Here, it is necessary to mention that a very small percentage of swept source should be directed into a Mach-Zehnder interferometer (MZI) to resample the interference signal at equal k-spacing or frequency spacing which is requisite by Fourier transform. Typically, balance detection is used in SS-OCT. It improves the dynamic range and also reduces auto-correlation noise, intensity noise from the tissue sample, fixed-pattern noise generated from the reference light [58]. Figure 2.10 illustrates an example of balanced detection. By a 90/10 coupler the swept source is divided into two arms. By which 90% of the power is guided to sample arm and rest 10% of the power to reference arm. Thus, the interference signal is acquired by two optical circulators at both output nodes of 2×2 coupler is focused into the balance detector.

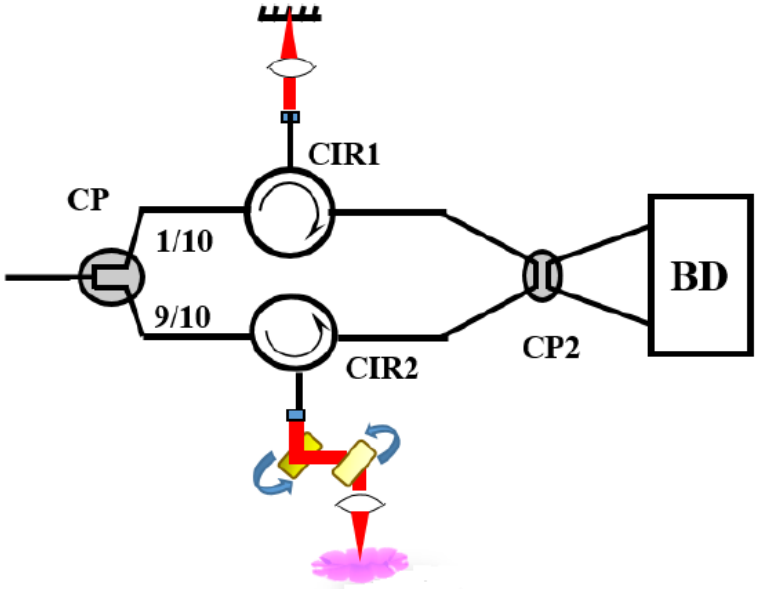

Figure 2.10: Graphic representation of imaging part by balance detection [58].

The swept laser have the greatest importance for SS-OCT system in the subsequent traits: sweep repetition rate, wavelength sweep range, linearity of power, sweep and more importantly instantaneous line width [58]. It would considerably influence the performance of system by image acquisition time, axial resolution, ranging depth, sensitivity and calibration difficulty. One of the most commonly used swept source laser is FDML laser (Fourier domain mode-locked), which provides a far better performance in all traits described above [59].

SS-OCT have an advantage in sensitivity as comparing with the time domain OCT, spectral domain OCT [59], as well as the imaging speed advantage is also have a keen importance for imaging in biomedical applications. It can remove the produced artifact due to sample motion and hence save time in imaging of sample in clinical environments. Larger roll-off performance is another advantage which improves the detection range that has a great significance in cardiovascular based applications as well as in skin cancer diagnosis.

2.5 OCT System Parameter

2.5.1 Axial Resolution

An OCT system axial resolution is depends upon the amount of coherence length (l_c) of the light source and is not depends upon the system optics. The distance travel by the

electromagnetic wave while maintaining the phase periodicity is known as coherence length 'l_c' of a light source and can be represented as [48]:

$$l_c = c.\, t_c \tag{2.12}$$

where c = speed of light and t_c = the coherence time

However, the coherence time t_c can be defined as:

$$t_c = \frac{\lambda^2}{c \cdot \Delta\lambda} \tag{2.13}$$

here λ and $\Delta\lambda$ is representing center wavelength and bandwidth of the light source, respectively. Equations 2.12 and 2.13 can be collectively represented as:

$$l_c = \frac{\lambda^2}{\Delta\lambda} \tag{2.14}$$

In OCT, generally the light source is considered as Gaussian by nature, thus for an OCT system axial resolution Δz can be characterized by the coherence length of a Gaussian light source [29]:

$$\Delta z = \frac{2\ln 2}{\pi}\frac{\lambda^2}{\Delta\lambda} \tag{2.15}$$

A high value of axial resolution can be achieved, if interference arises over a short distance as much as possible. As described in Equation 2.15, light sources with large bandwidths have short coherence lengths. For that reason a SLD, which is a low coherence source of light has the axial resolution higher than the axial resolution of a high coherence light source like a laser. Figure 2.11 illustrate the relationship between the coherence length and the axial resolution of a light source, where the interference is generated between the reflected light coming back from a sample interface and the light coming from a scanning reference path, as shown in figure 2.11 (a). Interference is observed whenever the path lengths are coinciding to within the range of the coherence length of the source of light. As shown in Figure 2.11 (b), a laser source with high coherence produces interference which can be detected over a large distance but it does not give any information about sample interface location. Whereas interference generated by a light source with low coherence over a short distance, clearly gives the information of sample interface position, when the acquired interference is demodulated, as shown in figure 2.11 (c).

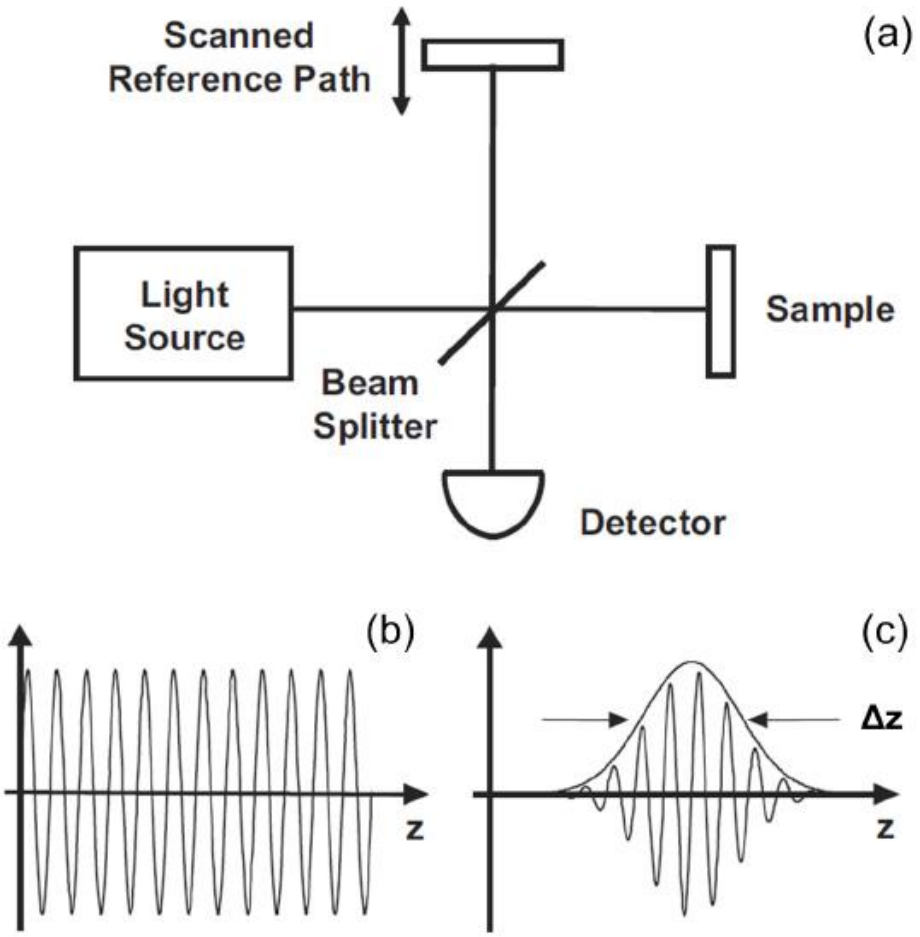

Figure 2.11: Schematic of a (a) TD-OCT setup and the relationship between the coherence length and the axial resolution of a light source (b) Low axial resolution when coherence length of light source is high (c) High axial resolution when the coherence length of light source is low [60].

For a Fourier domain OCT system, the maximum axial measurement range i.e. z_{max} can be associated to the axial resolution Δz as follows [31]:

$$z_{max} = \frac{\Delta z}{2} \cdot \frac{N}{2} \tag{2.16}$$

Where, N is representing the number of pixels in the spectrometer. Since, in real spectrum Fourier transform has conjugate symmetry with a zero delay; therefore N is divided by two. Based on Nyquist condition, the pixel spacing is selected as $\frac{\Delta z}{2}$. This equation exhibits that for a certain bandwidth of a light source, the number of pixels of a detector in the spectrometer are the measure of the maximum axial depth.

2.5.2 Lateral Resolution

The lateral resolution Δx in an OCT system is dependent on the objective lens used and is calculated using [48]:

$$\Delta x = \frac{1.22\, f\lambda}{D} = \frac{0.61\lambda}{NA} \tag{2.17}$$

where, f = focal length of lens,

λ = center wavelength of the light source,

D = diameter of lens,

NA = numerical aperture of the lens.

Numerical aperture is given by:

$$\text{NA} = n\sin\theta \tag{2.18}$$

Where n = refractive index of sample or imaging medium

θ = aperture angle

The lateral resolution is inversely proportional to the numerical aperture of the lens [60]. In most of the OCT imaging applications is a low value of numerical aperture is being selected, because most of the light energy spread deeper inside the tissue sample for a higher imaging depth. A trade-off is found between field depth and lateral resolution.

Chapter 3

EXPERIMENTAL DETAILS

Swept source optical coherence tomography (SS-OCT) system (OCS- 1300SS; Thorlabs, Dachau, Germany) used for studying the characteristics of normal and burn skin is shown in figure 3.1 [61].

Figure 3.1: Swept-source OCT system (OCS- 1300SS, Thorlabs) [61].

The central wavelength of the swept source is 1310 nm. The output power of the source is 10 mW and sweeping rate is 16 kHz (A-scans). The SS-OCT system is based on a Mach Zehnder interferometer, where the light from the reference and the sample arms interference. A stationary mirror is placed in the reference arm of the interferometer; the light reflected from the reference mirror is coupled with light reflected from the sample arm. The interferometric signal is recorded by a single photo-detector as a function of time. The sample is placed on the X-Y-Z rotational-translational stage. Microscopic view of the sample has been recorded by the CCD camera. A pair of two axis galvo mirror is used to scan the sample in the X-Y direction, which provides lateral and transverse scanning and create 1D, 2D or 3D images. A high-transimpedance, gain-balanced photo-detector is used to detect the interferometric signals which suppress autocorrelation noise and DC present in the interferometric signals. This OCT interferometric signal is sampled by a 14bit digitizer. The depth-dependent reflectivity profile for the OCT image can be obtained by taking the fast Fourier transform of the signal which will convert time domain signal into frequency domain.

The present system has maximum theoretical imaging depth of 3 mm, an axial resolution of 12µm and transverse resolution is 25 µm in air. The real imaging depth in sample is lower than in air, due to scattering effects. All the images recorded in this experiment is size of 1024 pixels (lateral) and 512 pixels in axial. Images from OCT are combinations of different backscattering lines (A-scans), one for each transverse scanning along a B-scan. Each A-scan can be analysed individually by performing a one-dimensional (1-D) characterization. The amplitude of the OCT signal reflectivity or backscattered intensity decay along the depth.

3.1 Methodology

3.1.1 Computational Method

The computational investigation is based on extracting an individual A-line (with dB unit in log scale) from OCT images. The whole process is properly explained in figure 3.1 with a typical A-line from the OCT imaging of normal skin sample.

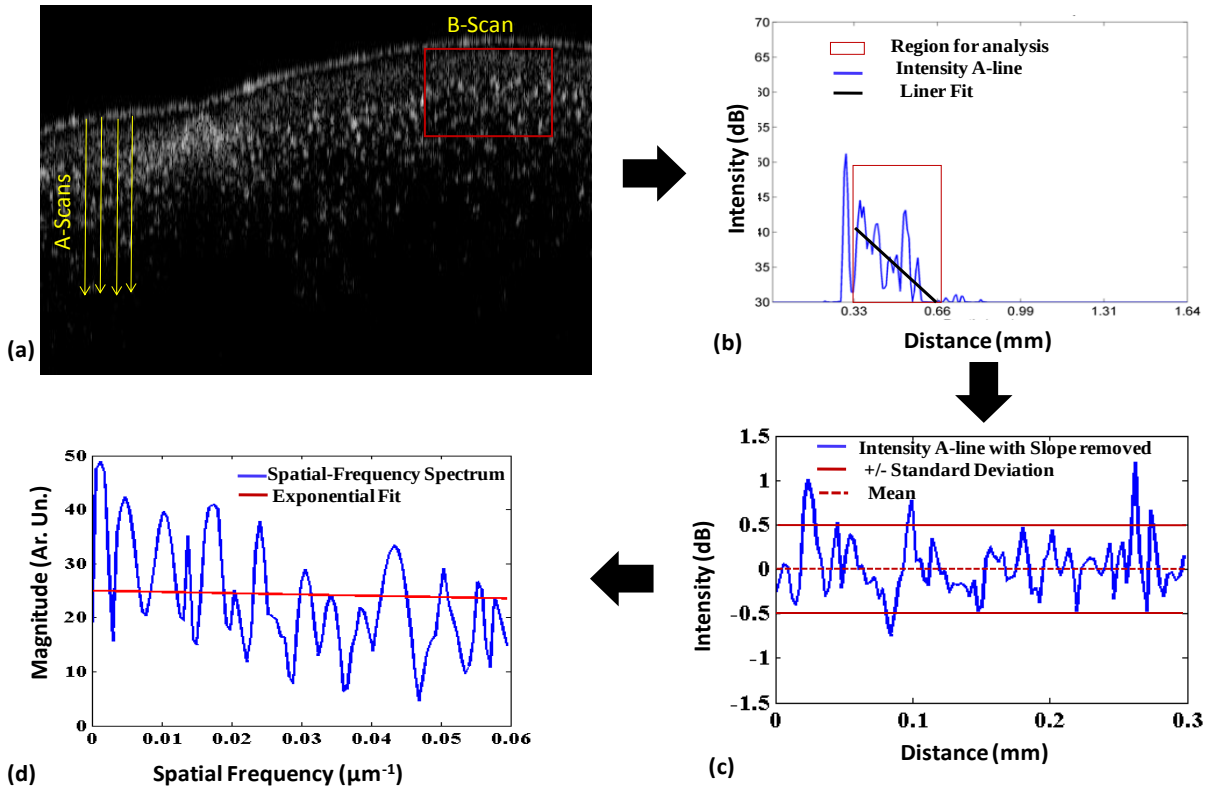

Figure 3.2: (a) shows the OCT image of normal skin sample, (b) A-line from OCT image with region of analysis, (c) STD of the signal after removed slope and (d) spatial frequency spectrum with exponential fit to calculate the exponential decay.

To quantify the changes in the backscattered light or OCT intensity of normal and burn skin we measure the attenuation coefficients from Beer-Lambert law [62]. Thus the OCT intensity is expressed by [62].

$$I = I_0 e^{-\mu z} \tag{3.1}$$

Equation (3.1) shows the intensity decays induced by the sample, relatively large intensity occurs at the air-sample interface. To avoid this effect we choose starting point of the analysis 10 pixel below air-sample interface as shown in figure. 3.2 (a). An axial region 0.3 mm is selected for A-line processing and the region of analysis is remains constant over the processing for all the samples. Figure 3.2 (b) shows the A-lines correspond to figure 3.2 (a). The attenuation property of the light depends upon the birefringence property of the sample. To extract the slope parameter to characterize the sample we fit linear line on each A-line. As the linear line in subtracted from the A-line the slope information from A-line is removed and the mean of the signal is approximately is zero as shown in the figure 3.2 (c).

3.1.2 B-Scan analysis or Texture analysis

As the mean of the signal is zero we calculate the fluctuation in the intensity signal, which is standard deviation. Standard deviation is the second parameter to evaluate the difference between normal and burn skin sample. To evaluate the amplitude information of the spatial frequency spectrum we took a Fourier transform of the intensity signal and the exponential fit the curve ($y = Ae^{-Bx}$). The exponential decay coefficient B is the third parameter to evaluate the difference between normal and burn skin. The quantitative representation of the A-line slope, the standard deviation of the slope-removed A-line, and the exponential decay coefficient of its spatial frequency spectrum parameters are presented in the figure 3.2 (d). The inherent structural and morphological changes that occur along the transverse direction can't be easily detected in A-san analysis but it can be detected in pixel distribution. A two-dimensional (2-D) texture analysis is used which can be useful in finding the pixels distribution. A 2D OCT image or B-scan image (as shown in figure 3.2 (a)) is a combination of number of A-scan backscattering profiles. The texture of images changes according to the spatial distribution of the intensities. Haralik *et al* developed Gray-Level Co-Occurrence Matrix (GLCM) analysis method for texture analysis [63]. The GLCM is formed from the segment of the image at a specified pixel distance and direction by counting the number of

occurrences of gray level adjacent to another gray level. Rows and column of the matrix representing the gray levels and the elements of the matrix probability of gray level co-occurrence. GLCM entries are basically based on comparing the pixels at a given displacement. Hence, the selection of displacement can greatly affect the result; especially the image displays a particular spatial orientation or repeating pattern. This is the main cause for using several different displacements for generating multiple GLCMs for a given sub-image of OCT image as shown in figure 3.2 (a). We computed GLCMs for four of the possible eight neighbour connected pixels, consisting of 0°, 45°, 90°, and 135°, one-pixel offsets relative to the central pixel for 2D OCT sub-images. We calculate four most potential statistical features such as contrast, correlation, (also called variance or inertia), energy (also called uniformity or angular second moment), and homogeneity from each GLCM. The maximum and minimum values of all the parameters are +1 and 0 or -1 [63]. These features are given in Eq. (3.2) to Eq. (3.5)

$$Contrast = \sum_{i,j} |i-j|^2 p(i,j), \tag{3.2}$$

$$Correlation = \sum_{i,j} \frac{(i-\mu_i)(j-\mu_j)[p(i,j)]}{\sigma_i \sigma_j}, \tag{3.3}$$

$$Energy = p(i,j)^2, \tag{3.4}$$

$$Homogeneity = \frac{p(i,j)}{1+|i-j|}, \tag{3.5}$$

In the above equations, i and j refer to the intensity bins in the GLCM, $p(i,j)$ refers to the probability of gray level i occurring to the next gray level j, and μ_i, σ_i and μ_j, σ_j refer to the mean and variance of the ith and jth rows and columns of the GLCM. Thus, 16 GLCM features are evaluated for each 2D OCT sub-image. Once the GLCM is computed and normalized, the joint probability density can be computed. From that Contrast, correlation, energy, and homogeneity matrices are derived. High contrast is an indication of that an image has high number of pixels pairs which has large difference in a gray level at the specified separation and orientation. High correlation occurs in an image with periodic or constant features. Energy will be higher for those images which have uniform gray level and high homogeneity represent the absence of intra- regional change. Combining the Computational parameters and GLCM parameters resulted in a total of 7 parameters to describe each single image.

3.1.3 Image Classification

The features of the normal and burn skin sample were compared. In order to improve the identification accuracy a classification algorithm based on support vector machine (SVM) is utilized [64]. SVM has been extensively used for pattern classification. It has number of advantages compared to conventional pattern classification algorithm such as it can conduct classification on a very small amount of training samples and features space can be high dimensional also. It's chosen as the classification algorithm as it out performs other conventional pattern classification methods logistic regression algorithm [64]. For SVM classification input is known as feature vector and output is known as class label. The details of SVM can be found out at Reference [64]. Training was performed on 64% of the data selected at random.

CHAPTER 4

RESULTS AND DISCUSSIONS

In this study, we compute seven parameters to clarify the dissimilarity between the OCT images of normal and burn skin/tissue. Twenty burn and normal skin samples were taken for the study. Figure 4.1 (a) and figure 4.2 (a) shows the normal and burn skin and an area of region is marked and each time the same region is used to extract the information. The volume of each sample is 512 x 512 x 1024 pixels^3. Figure 4.1(a – d) and figure 4.2 (a – d) depicts an OCT image (B-scan) formed by backscattering lines or A-scans for normal and burn skin, respectively.

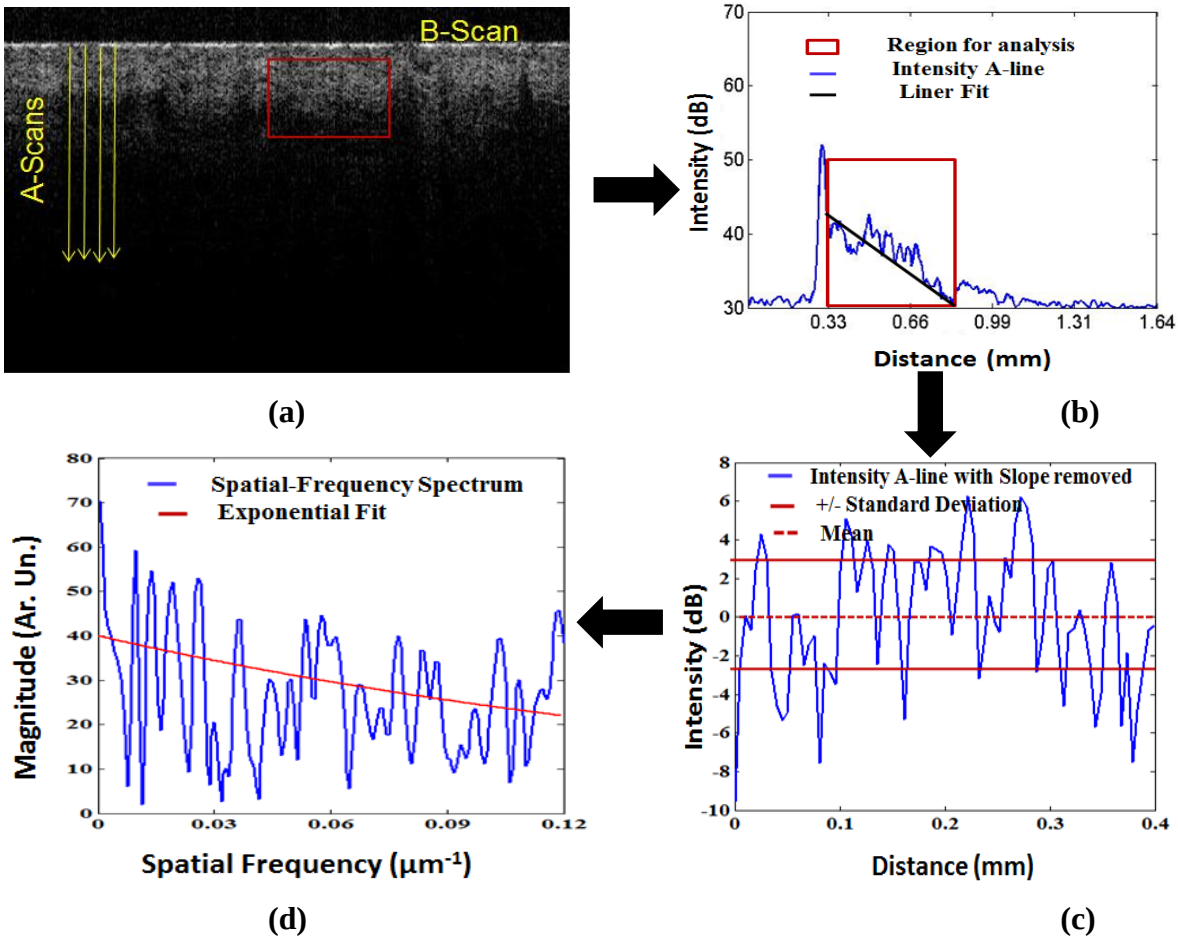

Figure 4.1: (a) shows the OCT image of normal skin, (b) A-line from OCT image with region of analysis, (c) STD of the signal after removed slope and (d) spatial frequency spectrum with exponential fit to calculate the exponential decay.

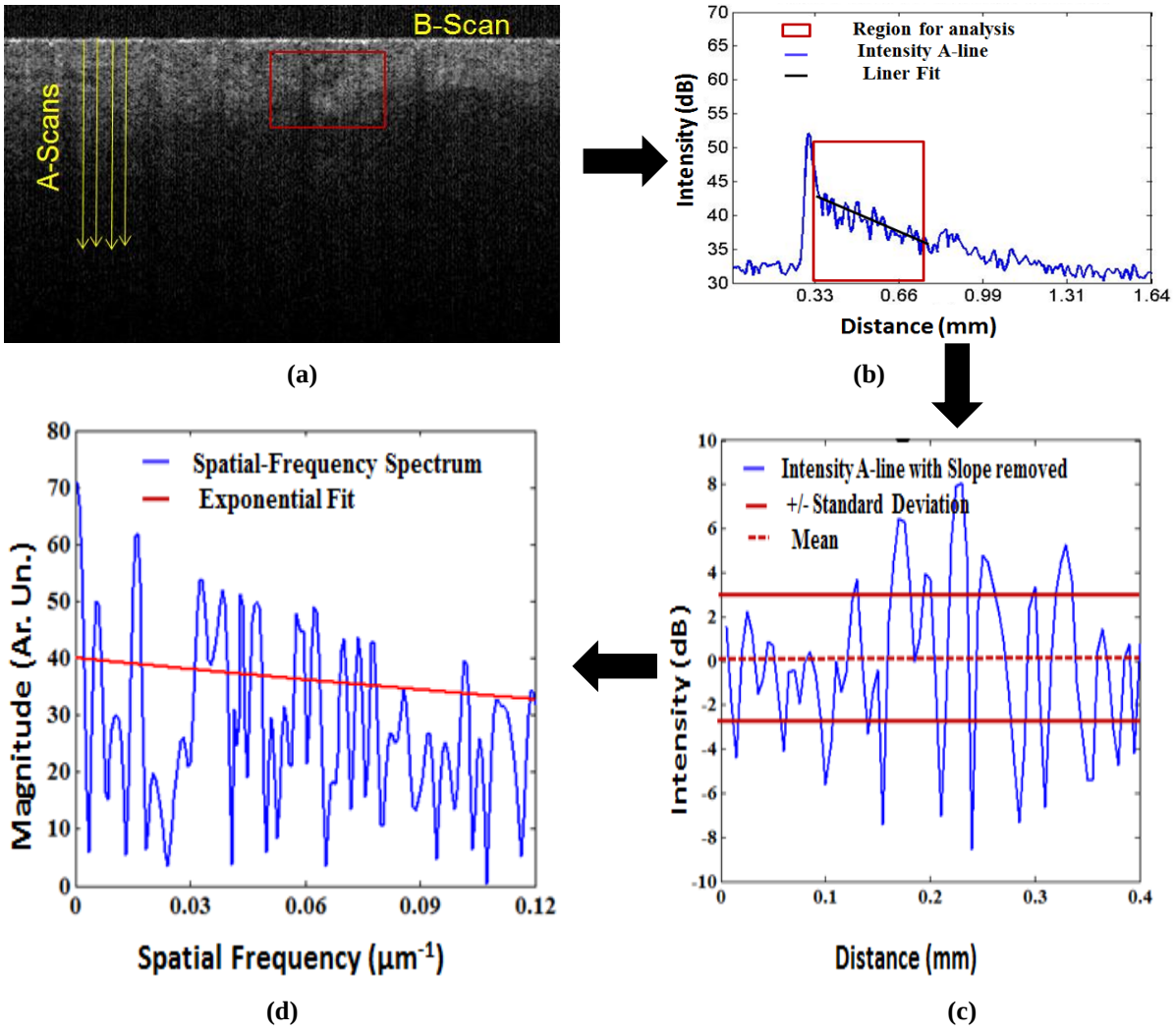

Figure 4.2: (a) shows the OCT image of burn skin, (b) A-line from OCT image with region of analysis, (c) STD of the signal after removed slope and (d) spatial frequency spectrum with exponential fit to calculate the exponential decay.

From the OCT images, the depth-dependent reflectivity profile A-line (dB unit in log scale) is obtained. Along the depth the amplitude of the OCT signal reflectivity decreases figure 4.1 (a – d) shows the *in-vivo* images of the sample/normal skin. To evaluate the attenuation coefficients we averages 100 B- scan images and 100 adjacent A-lines , which corresponds to 232 µm in the lateral distance, which shows the statistical result of the sample or normal skin. Similar, analysis has been performed for burn skin, which is shown in figure 4.2 (a – d) for all 20 samples. We found that the attenuation coefficient is more on burn as compared to normal tissue/skin.

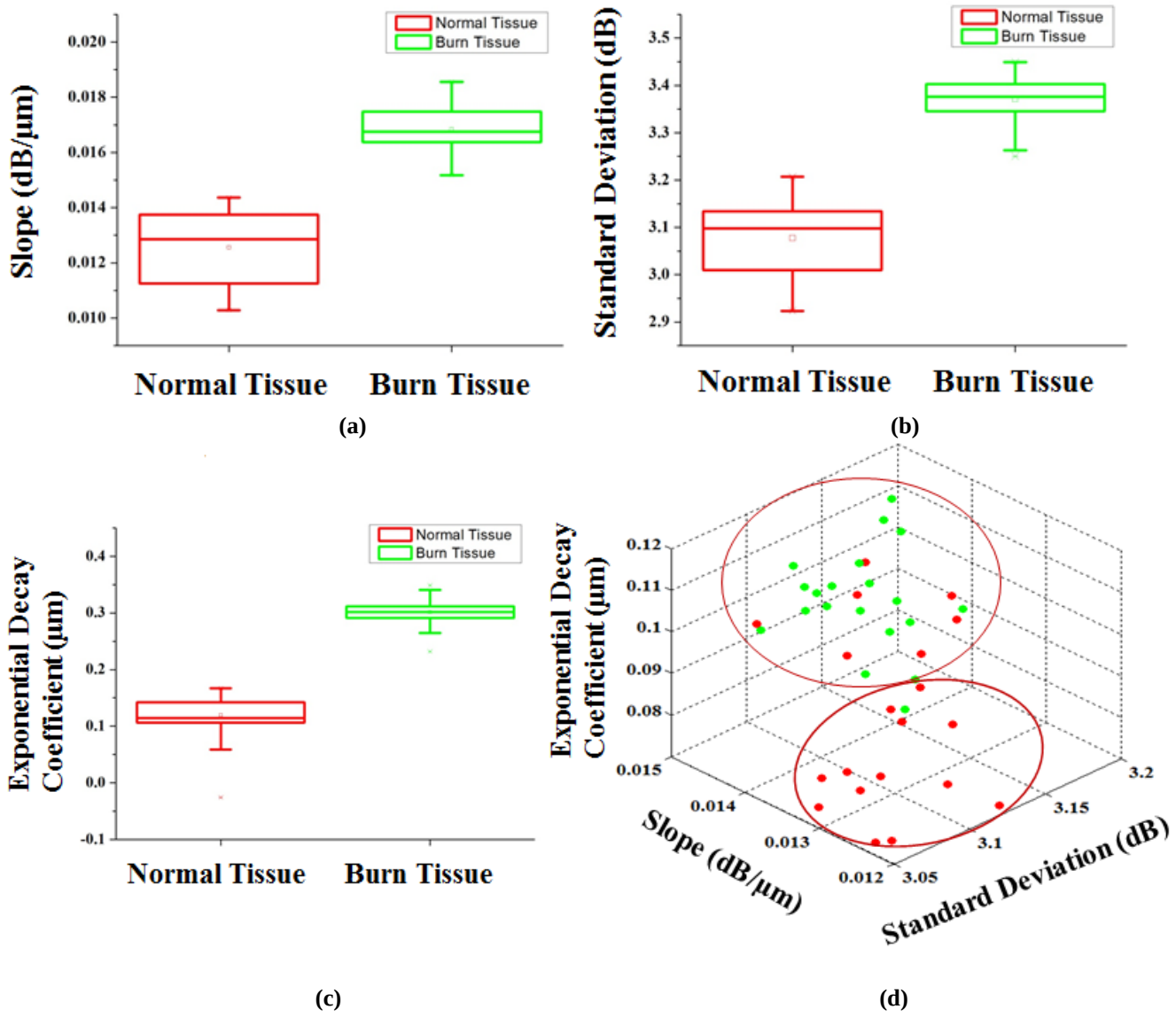

Figure 4.3: (a) Box plot for A-line slope (b) box plot of standard deviation removed A-line, (c) box plot for exponential decay coefficient of the spatial frequency spectrum of the slope removed A-line (d) 3D plot of all the data point of normal and burn skin/tissue sample in the spatial region by composition of A-line slope, standard deviation of slope removed A-line and exponential decay coefficient of standard deviation of slope removed A-line with 80% confidence ellipsoid.

It can be seen that attenuation coefficient increases in burn skin resulting from reduced backscattered intensity due to formation of collagen which changes the birefringence as shown in figure 4.3 (a). The slope value for A-lines are quantified as 0.013 ± 0.002 dB⁄μm and 0.017 ± 0.002 dB⁄μm for normal skin and burn skin, respectively as shown in the figure 4.3 (a). The higher absolute value of slope for burn skin compared to normal skin is an indication of higher attenuation of light for the same penetration depth.

The fluctuation in intensity signal or standard deviation is larger for normal skin compared to burn tissue are 3.10 ± 0.11 dB and 3.37 ± 0.07 dB, respectively as shown in figure 4.3 (b). The higher standard deviation for burn tissue as compared to normal tissue is an indication of higher variation of birefringence along the depth. The exponential decay coefficient obtained for normal tissue and burn tissue are 0.11 ± 0.06 µm and 0.31 ± 0.04 µm, respectively as shown in figure 4.3 (c). The exponential decay coefficient is an indication of that in burn tissue; sample has more low frequency component along the depth as compared to normal tissue. All the three parameters will be helpful in differentiate of tissues. By combining all the three parameters we will get 3-D information, which gives their relative positions as shown in figure 4.3 (d).

To evaluate all the four parameters contrast, correlation, energy and homogeneity for texture analysis for all the samples with the help of GLCM we averaged 100 B-scan images. The contrast obtained is quantified as 2.4 ± 0.9 and 4.5 ± 1.9, respectively for burn and normal tissue/skin, as shown in the figure 4.4 (a). Contrast is higher for normal tissue as compared to burn tissue is an indication of large difference in a gray level at the specified separation and orientation for sample, which is basically due to more collagen content present on the burn tissue/skin as compare to normal tissue/skin. The correlation obtained is quantified as 0.12 ± 0.09 and 0.08 ± 0.05, respectively for burn and normal tissue/skin, as shown in the figure 4.4 (b). Correlation is higher for burn tissue as compared to normal tissue is an indication that burn tissue sample images have more periodic or constant features.

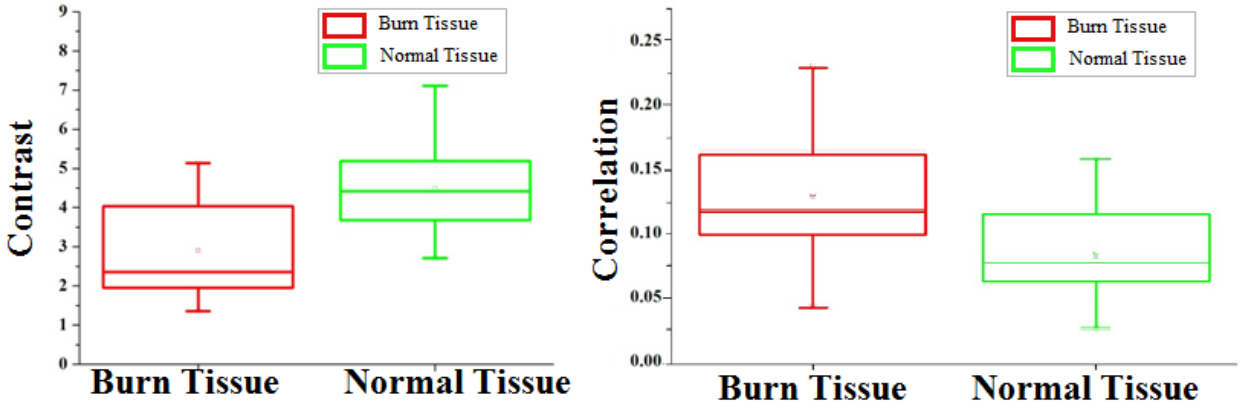

(a) (b)

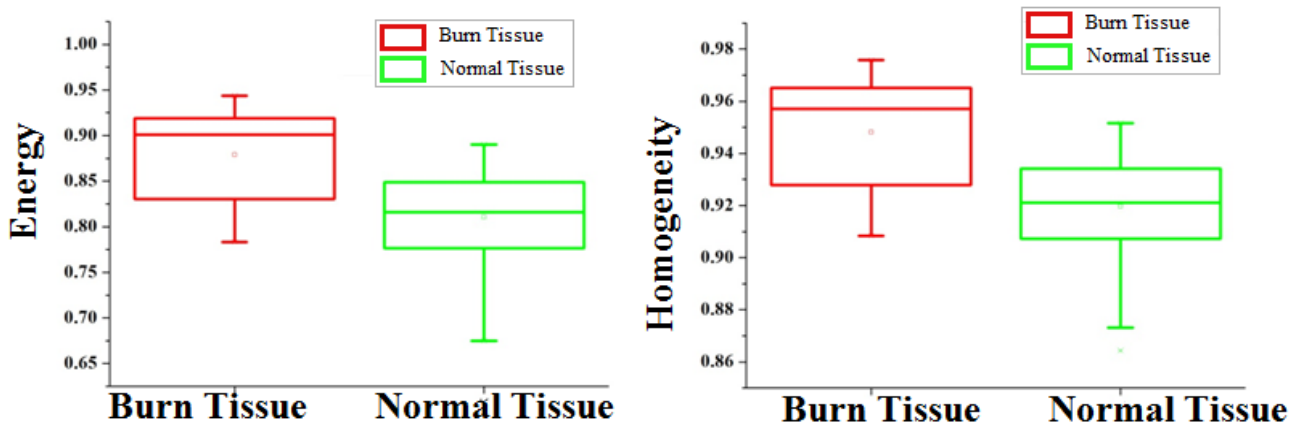

(c) (d)

Figure 4.4: Box plot for (a) contrast (b) correlation, (c) energy and (d) homogeneity computed with the help of GLCM.

The energy obtained is quantified as 0.90 ± 0.04 and 0.81 ± 0.06, respectively for burn and normal tissue/skin, as shown in the figure 4.4 (c). Energy is higher for burn tissue/skin as compared to normal tissue/skin is an indication that images have uniform gray level. The homogeneity obtained is quantified as 0.95 ± 0.02 and 0.92 ± 0.03, respectively for burn and normal tissue/skin, as shown in the figure 4.4 (d). Homogeneity is higher for burn as compared to normal tissue is an indication that images have absence of intra- regional change uniform gray level.

Now the feature vector has been obtained and normalized. Multi-class SVM with Gaussian kernel is utilized for classification and all the seven parameters A-line slope, the standard deviation of the slope-removed A-line, and the exponential decay coefficient of its spatial frequency spectrum, contrast, correlation, energy and homogeneity are treated as different parameters of feature vector of the SVM. Out of 40 samples, 28 samples are randomly selected; constituting 196 data points in the training and 12 samples are as test database in total. The test data result obtained from trained model. The accuracy obtained from SVM is 92.41%. With the help of SVM we can classify in between normal and burn tissue. This method leads to a speedy quality assessment. The quantification based on these seven parameters provides more consistent information as compare to only observation. Further, to increase its efficiency we have to increase the number of samples.

CHAPTER 5

CONCLUSION

We have demonstrated an automated computational and texture analysis method to analyse OCT images for the investigation of burns/abnormalities in human skin in a non-invasive manner with the help of SVM. The three computational parameters A-line slope, the standard deviation of the slope-removed A-line, and the exponential decay coefficient of its spatial frequency spectrum, and four texture parameters contrast, correlation, energy and homogeneity are used as feature vector of SVM for the classification of normal and burn skin tissue sample. This automated method can be used to measure the structural changes occurs in normal skin after burn.

References

[1] B. W. Graf, and S. A. Boppart, "Imaging and analysis of three-dimensional cell culture models," Methods in molecular biology (Clifton, N.J.) **591**, 211-227 (2010).

[2] D. Levitz, M. T. Hinds, A. Ardeshiri, S. R. Hanson, and S. L. Jacques, "Non-destructive label-free monitoring of collagen gel remodelling using optical coherence tomography," Biomaterials **31**, 8210-8217 (2010).

[3] K. Licha, and C. Olbrich, "Optical imaging in drug discovery and diagnostic applications," Advanced Drug Delivery Reviews **57**, 1087-1108 (2005).

[4] P. N. Prasad, Introduction to bio photonics (Wiley-Interscience, Hoboken, NJ, 2003).

[5] A. R. Webb, Introduction to biomedical imaging (Wiley, Hoboken, New Jersey, 2003).

[6] C. M. C. Tempany, and B. J. McNeil, "Advances in Biomedical Imaging," JAMA: The Journal of the American Medical Association **285**, 562-567 (2001).

[7] J. G. Fujimoto, "Optical coherence tomography for ultrahigh resolution in vivo imaging," Nature Biotechnology **21**, 1361-1367 (2003).

[8] C. Balas, "Review of biomedical optical imaging – A powerful, non-invasive, nonionizing technology for improving in vivo diagnosis," Measurement Science and Technology **20** (2009).

[9] W. R. Hendee, "Cross sectional medical imaging: a history," Radio-graphics: a review publication of the Radiological Society of North America **9**, 1155-1180 (1989).

[10] P. N. T. Wells, "Ultrasound imaging," Physics in Medicine and Biology **51**, R83 - R98 (2006).

[11] J. G. Fujimoto, and D. L. Farkas, Biomedical optical imaging (Oxford University Press, Oxford; New York, 2009).

[12] B. Taouli, M. Losada, A. Holland, and G. Krinsky, "Magnetic resonance imaging of hepatocellular carcinoma," Gastroenterology **127**, S144-S152 (2004).

[13] J. W. Bailet, J. A. Sercarz, E. Abemayor, Y. Anzai, R. B. Lufkin, and C. K. Hoh, "The use of positron emission tomography for early detection of recurrent head and neck squamous cell carcinoma in post radiotherapy patients," Laryngoscope **105**, 135-139 (1995).

[14] R. A. Robb, "Biomedical Imaging: Past, Present and Predictions," Mayo Clinic College of Medicine.

[15] M. Moller, P. Kalebo, G. Tidebrant, T. Movin, and J. Karlsson, "The ultrasonographic appearance of the ruptured Achilles tendon during healing: A longitudinal evaluation of surgical and nonsurgical treatment, with comparisons to MRI appearance," Knee Surgery, Sports Traumatology, Arthroscopy **10**, 49-56 (2002).

[16] G. Bosch, P. René van Weeren, A. Barneveld, and H. T. M. van Schie, "Computerised analysis of standardised ultrasonographic images to monitor the repair of surgically created core lesions in equine superficial digital flexor tendons following treatment with intratendinous platelet rich plasma or placebo," Veterinary Journal **187**, 92 - 98 (2011).

[17] K. Jeyapalan, M. A. Bisson, J. J. Dias, Y. Griffin, and R. Bhatt, "The role of ultrasound in the management of flexor tendon injuries," Journal of Hand Surgery: **33**, 430-434 (2008).

[18] A. Shalabi, "Magnetic resonance imaging in Chronic Achilles Tendinopathy," Acta Radiologica **45**, 1- 45 (2004).

[19] B. A. Kumar, A. R. Tolat, G. Threepuraneni, and B. Jones, "The role of magnetic resonance imaging in late presentation of isolated injuries of the flexor digitorum pro fundus tendon in the finger," Journal of Hand Surgery **25 B**, 95-97 (2000).

[20] U. G. Longo, A. Lamberti, N. Maffulli, and V. Denaro, "Tissue engineered biological augmentation for tendon healing: A systematic review," British Medical Bulletin **98**, 31-59 (2011).

[21] W. Tan, A. L. Oldenburg, J. J. Norman, T. A. Desai, and S. A. Boppart, "Optical coherence tomography of cell dynamics in three-dimensional tissue models," Optics Express **14**, 7159-7171 (2006).

[22] H. Xu, S. F. Othman, L. Hong, I. A. Peptan, and R. L. Magin, "Magnetic resonance microscopy for monitoring osteogenesis in tissue-engineered construct in vitro," Physics in Medicine and Biology **51**, 719-732 (2006).

[23] H. Xu, S. F. Othman, and R. L. Magin, "Monitoring Tissue Engineering Using Magnetic Resonance Imaging," Journal of Bioscience and Bioengineering **106**, 515-527 (2008).

[24] A. T. Yeh, B. Kao, W. G. Jung, Z. Chen, J. S. Nelson, and B. J. Tromberg, "Imaging wound healing using optical coherence tomography and multiphoton microscopy in an in vitro skin-equivalent tissue model," Journal of Biomedical Optics **9**, 248-253 (2004).

[25] J. W. Strickland, "The scientific basis for advances in flexor tendon surgery," Journal of Hand Therapy **18**, 94-111 (2005).

[26] L. V. Wang, and H.-i. Wu, Biomedical optics: principles and imaging (Wiley-Interscience, Hoboken, N.J., 2007).

[27] R. R. Alfano, S. G. Demos, and S. K. Gayen, "Advances in Optical Imaging of Biomedical Media," Annals of the New York Academy of Sciences **820**, 248-271 (1997).

[28] C. Pitris, M. E. Brezinski, B. E. Bouma, G. J. Tearney, J. F. Southern, and J. G. Fujimoto, "High resolution imaging of the upper respiratory tract with optical coherence tomography: A feasibility study," American Journal of Respiratory and Critical Care Medicine **157**, 1640-1644 (1998).

[29] B. E. Bouma, and G. J. Tearney, Handbook of optical coherence tomography (Marcel Dekker, New York, 2002).

[30] Alfaro D: Age-related macular degeneration: a comprehensive textbook. Lippincott Williams & Wilkins; (2005).

[31] M. E. Brezinski, Optical Coherence Tomography: Principles and Applications (Academic Press, 2006).

[32] G. Häusler, and M. W. Lindner, ""Coherence radar" and "spectral radar" – New tools for dermatological diagnosis," Journal of Biomedical Optics **3**, 21-31 (1998).

[33] R. Leitgeb, C. K. Hitzenberger, and A. F. Fercher, "Performance of Fourier domain vs. time domain optical coherence tomography," Optics Express **11**, 889-894 (2003).

[34] M. Wojtkowski, R. Leitgeb, A. Kowalczyk, T. Bajraszewski, and A. F. Fercher, "In vivo human retinal imaging by Fourier domain optical coherence tomography," Journal of Biomedical Optics **7**, 457-463 (2002).

[35] J. F. De Boer, B. Cense, B. H. Park, M. C. Pierce, G. J. Tearney, and B. E. Bouma, "Improved signal-to-noise ratio in spectral-domain compared with time-domain optical coherence tomography," Optics Letters **28**, 2067-2069 (2003).

[36] M. A. Choma, M. V. Sarunic, C. Yang, and J. A. Izatt, "Sensitivity advantage of swept source and Fourier domain optical coherence tomography," Optics Express **11**, 2183 - 2189 (2003).

[37] S. H. Yun, G. J. Tearney, B. E. Bouma, B. H. Park, and J. F. De Boer, "High-speed spectral-domain optical coherence tomography at 1.3 um wavelength," Optics Express **11**, 3598-3604 (2003).

[38] R. Leitgeb, W. Drexler, A. Unterhuber, B. Hermann, T. Bajraszewski, T. Le, A. Stingl, and A. Fercher, "Ultrahigh resolution Fourier domain optical coherence tomography," Optics Express **12**, 2156-2165 (2004).

[39] D. P. Popescu, C. Flueraru, Y. Mao, S. Chang, J. Disano, S. Sherif, and M. G. Sowa, "Optical coherence tomography: fundamental principles, instrumental designs and biomedical applications," Biophysical Reviews **3**, 155-169 (2011).

[40] C. Mason, and et al., "The potential of optical coherence tomography in the engineering of living tissue," Physics in Medicine and Biology **49**, 1097 (2004).

[41] W. Drexler, and J. G. Fujimoto, "Optical coherence tomography technology and applications," Springer (2008).

[42] W. Jung, J. Zhang, J. Chung, P. Wilder-Smith, M. Brenner, J. S. Nelson, and Z. Chen, "Advances in oral cancer detection using optical coherence tomography," IEEE Journal on Selected Topics in Quantum Electronics **11**, 811-816 (2005).

[43] R. N. Graf, F. E. Robles, X. Chen, and A. Wax, "Detecting precancerous lesions in the hamster cheek pouch using spectroscopic white-light optical coherence tomography to assess nuclear morphology via spectral oscillations," Journal of Biomedical Optics **14**, 064030 (2009).

[44] X. Liang, B. W. Graf, and S. A. Boppart, "Imaging engineered tissues using structural and functional optical coherence tomography," Journal of Biophotonics **2**, 643- 655 (2009).

[45] A. M. Rich, M. I. Nataatmadja, and P. C. Reade, "Basal cell nuclear size in experimental oral mucosal carcinogenesis," British Journal of Cancer **64**, 96-98 (1991).

[46] G. L. Tipoe, F. H. White, and C. J. Pritchett, "A morphometric study of histological variations during cellular differentiation of normal human colorectal epithelium," Journal of Anatomy **181**, 189-197 (1992).

[47] P. H. Tomlins, and R. K. Wang, "Theory, developments and applications of optical coherence tomography," Journal of Physics D: Applied Physics **38**, 2519-2535 (2005).

[48] W. Tan, A. L. Oldenburg, J. J. Norman, T. A. Desai, and S. A. Boppart, "Optical coherence tomography of cell dynamics in three-dimensional tissue models," Optics Express **14**, 7159-7171 (2006).

[49] D. Huang, E. A. Swanson, C. P. Lin, J. S. Schuman, W. G. Stinson, W. Chang, M. R. Hee, T. Flotte, K. Gregory, C. A. Puliafito, and J. G. Fujimoto, "Optical coherence tomography," Science **254**, 1178-1181 (1991).

[50] Z. Wang, H. Pan, Z. Yuan, J. Liu, W. Chen, and Y. Pan, "Assessment of dermal wound repair after collagen implantation with optical coherence tomography," Tissue Engineering - Part C: Methods **14**, 35-45 (2008).

[51] M. Wojtkowski, B. L. Sikorski, I. Gorczynska, M. Gora, M. Szkulmowski, D. Bukowska, J. KaÅ‚uzny, J. G. Fujimoto, and A. Kowalczyk, "Comparison of reflectivity maps and outer retinal topography in retinal disease by 3-D Fourier domain optical coherence tomography," Optics Express **17**, 4189-4207 (2009).

[52] B. Potsaid, I. Gorczynska, V. J. Srinivasan, Y. Chen, J. Jiang, A. Cable, and J. G. Fujimoto, "Ultrahigh speed spectral / Fourier domain OCT ophthalmic imaging at 70,000 to 312,500 axial scans per second," Optics Express **16**, 15149-15169 (2008).

[53] A. M. Rollins, M. D. Kulkarni, S. Yazdanfar, R. Ung-Arunyawee, and J. A. Izatt, "In vivo video rate optical coherence tomography," Optics Express **3**, 219-229 (1998).

[54] R. Bracewell, the Fourier Transform and Its Applications (McGraw-Hill Science/Engineering/Math, 1999).

[55] Wojtkowski M, Srinivasan V, Fujimoto J, Ko T, Schuman J, Kowalczyk A, Duker J, "Three-dimensional retinal imaging with high-speed ultrahigh-resolution optical coherence tomography," Ophthalmology **112**, 1734-1746 (2005).

[56] Leitgeb R, Hitzenberger C, Fercher A, "Performance of Fourier domain vs. time domain optical coherence tomography," Optics Express **11**, 889-894 (2003).

[57] S. R. Chinn,E. A. Swanson, and J. G. Fujimoto, "Optical coherence tomography using a frequency-tunable optical source," Optics letter **22**, 340-342 (1997).

[58] W. Drexler, and J. G. Fujimoto, "optical coherence tomography applications," in Optical coherence tomography: technology and applications, New York: Springer Berlin Heidelberg, **7**, 209-238 (2008).

[59] R. Huber, M. Wojtkowski, and J. G. Fujimoto, "Fourier Domain Mode Locking (FDML): A new laser operating regime and applications for optical coherence tomography," Optics Express **14**, 3225-3237 (2006).

[60] D. Huang, J. Wang, C. P. Lin, C. A. Puliafito, and J. G. Fujimoto, "Micronresolution ranging of cornea anterior chamber by optical reflectometry," Lasers in Surgery and Medicine **11**, 419-425 (1991).

[61] http://www.thorlabs.com/images/TabImages/OCT_brochure_12_10.pdf.

[62] M. M. Mandurah, A. Sadr, Y. Kitasako, S. Nakashima,T. A. Bakhsh, J. Tagami and Y. Sumi, "Monitoring remineralization of enamel subsurface lesions by optical coherence tomography ," Journal of Biomedical Optics **18**, 046006-046011 (2013).

[63] R. M. Haralick, K. Shanmugam, and I. Dinstein, "Textural features for image classification," IEEE transaction on systems, man and cybernetics **6**, 610 – 621 (1973).

[64] Vapnik, Vladimir, E. G. Steven and A. Smola, “Support Vector Method for Function Approximation, Regression Estimation, and Signal Processing,” Advances in Neural Information Processing Systems **9**, 281-287 (1997).

PLAGIARISM CERTIFICATE

VR

ORIGINALITY REPORT

14%	2%	13%	3%
SIMILARITY INDEX	INTERNET SOURCES	PUBLICATIONS	STUDENT PAPERS

PRIMARY SOURCES

1	Wang, Shang. "Three-dimensional computational analysis of optical coherence tomography images for the detection of soft tissue sarcomas", Journal of Biomedical Optics, 2013. Publication	2%
2	Optical Coherence Tomography, 2015. Publication	2%
3	Submitted to University of Hong Kong Student Paper	1%
4	biomedicaloptics.spiedigitallibrary.org Internet Source	1%
5	Handbook of Coherent-Domain Optical Methods, 2013. Publication	1%
6	Real, Eusebio, Alma Eguizabal, Alejandro Pontón, Marta Calvo Díez, José Fernando Val-Bernal, Marta Mayorga, José M. Revuelta, José M. López-Higuera, and Olga M. Conde. "Optical coherence tomography assessment of vessel wall degradation in thoracic aortic aneurysms", Journal of	1%